The Astrophysical Journal, 825:132 (31pp), 2016 July 10 doi:10.3847/0004-637X/825/2/132

NuSTAR HARD X-RAY SURVEY OF THE GALACTIC CENTER REGION. II. X-RAY POINT SOURCES

JaeSub Hong[1], Kaya Mori[2], Charles J. Hailey[2], Melania Nynka[2], Shuo Zhang[2], Eric Gotthelf[2,3], Francesca M. Fornasini[4], Roman Krivonos[5], Franz Bauer[6,7,8], Kerstin Perez[9], John A. Tomsick[10], Arash Bodaghee[11], Jeng-Lun Chiu[10], Maïca Clavel[10], Daniel Stern[12], Jonathan E. Grindlay[1], David M. Alexander[13], Tsuguo Aramaki[14], Frederick K. Baganoff[15], Didier Barret[16,17], Nicolas Barrière[10], Steven E. Boggs[10], Alicia M. Canipe[2], Finn E. Christensen[16], William W. Craig[10,18], Meera A. Desai[2], Karl Forster[19], Paolo Giommi[20], Brian W. Grefenstette[19], Fiona A. Harrison[19], Dooran Hong[2], Allan Hornstrup[21], Takao Kitaguchi[22,23], Jason E. Koglin[24], Kristen K. Madsen[19], Peter H. Mao[19], Hiromasa Miyasaka[19], Matteo Perri[20,25], Michael J. Pivovaroff[18], Simonetta Puccetti[20,25], Vikram Rana[19], Niels J. Westergaard[21], William W. Zhang[26], and Andreas Zoglauer[10]

[1] Harvard-Smithsonian Center for Astrophysics, 60 Garden St., Cambridge, MA 02138, USA; jaesub@head.cfa.harvard.edu
[2] Columbia Astrophysics Laboratory, Columbia University, New York, NY 10027, USA
[3] Departament de Física Quàntica i Astrofísica, Institut de Ciències del Cosmos, Universitat de Barcelona, IEEC-UB, Martí i Franquès 1, 08028, Barcelona, Spain
[4] Astronomy Department, University of California, Berkeley CA 94720, USA
[5] Space Research Institute, Russian Academy of Sciences, Profsoyuznaya 84/32, 117997 Moscow, Russia
[6] Instituto de Astrofísica, Facultad de Física, Pontificia Universidad Catolica de Chile, 306, Santiago 22, Chile
[7] Millennium Institute of Astrophysics, Santiago, Chile
[8] Space Science Institute, 4750 Walnut Street, Suite 205, Boulder, CO 80301, USA
[9] Haverford College, 370 Lancaster Avenue, KINSC L109, Haverford, PA 19041, USA
[10] Space Sciences Laboratory, University of California, Berkeley, CA 94720, USA
[11] Georgia College, 231 W. Hancock St., Milledgeville, GA 31061, USA
[12] Jet Propulsion Laboratory, California Institute of Technology, Pasadena, CA 91109, USA
[13] Department of Physics, Durham University, Durham DH1 3LE, UK
[14] Standford National Accelerator Laboratory, 2575 Sand Hill Road, Menlo Park, CA 94025, USA
[15] Kavli Institute for Astrophysics and Space Research, Massachusets Institute of Technology, Cambridge, MA 02139, USA
[16] Université de Toulouse, UPS-OMP, IRAP, Toulouse, France
[17] CNRS, Institut de Recherche en Astrophysique et Planétologie, 9Av. colonel Roche, BP 44346, F-31028 Toulouse Cedex 4, France
[18] Lawrence Livermore National Laboratory, Livermore, CA 94550, USA
[19] Cahill Center for Astronomy and Astrophysics, California Institute of Technology, Pasadena, CA 91125, USA
[20] ASI Science Data Center, Via del Politecnico snc I-00133, Roma, Italy
[21] DTU Space—National Space Institute, Technical University of Denmark, Elektrovej 327, DK-2800 Lyngby, Denmark
[22] Department of Physical Science, Hiroshima University, Higashi-Hiroshima, Hiroshima 739-8526, Japan
[23] Core of Research for the Energetic Universe, Hiroshima University, Higashi-Hiroshima, Hiroshima 739-8526, Japan
[24] Kavli Institute for Particle Astrophysics and Cosmology, SLAC National Accelerator Laboratory, Menlo Park, CA 94025, USA
[25] INAF—Astronomico di Roma, via di Frascati 33, I-00040 Monteporzio, Italy
[26] NASA Goddard Space Flight Center, Greenbelt, MD 20771, USA
Received 2016 January 29; revised 2016 April 28; accepted 2016 May 12; published 2016 July 12

ABSTRACT

We present the first survey results of hard X-ray point sources in the Galactic Center (GC) region by *NuSTAR*. We have discovered 70 hard (3–79 keV) X-ray point sources in a 0.6 deg^2 region around Sgr A* with a total exposure of 1.7 Ms, and 7 sources in the Sgr B2 field with 300 ks. We identify clear *Chandra* counterparts for 58 *NuSTAR* sources and assign candidate counterparts for the remaining 19. The *NuSTAR* survey reaches X-ray luminosities of $\sim 4\times$ and $\sim 8 \times 10^{32}$ erg s^{-1} at the GC (8 kpc) in the 3–10 and 10–40 keV bands, respectively. The source list includes three persistent luminous X-ray binaries (XBs) and the likely run-away pulsar called the Cannonball. New source-detection significance maps reveal a cluster of hard (>10 keV) X-ray sources near the Sgr A diffuse complex with no clear soft X-ray counterparts. The severe extinction observed in the *Chandra* spectra indicates that all the *NuSTAR* sources are in the central bulge or are of extragalactic origin. Spectral analysis of relatively bright *NuSTAR* sources suggests that magnetic cataclysmic variables constitute a large fraction (>40%–60%). Both spectral analysis and log$N$–log$S$ distributions of the *NuSTAR* sources indicate that the X-ray spectra of the *NuSTAR* sources should have $kT > 20$ keV on average for a single temperature thermal plasma model or an average photon index of $\Gamma = 1.5$–2 for a power-law model. These findings suggest that the GC X-ray source population may contain a larger fraction of XBs with high plasma temperatures than the field population.

Key words: Galaxy: center – X-rays: binaries – X-rays: diffuse background – X-rays: general

1. INTRODUCTION

The high density stellar cluster around the super massive black hole (BH) at the center of the Milky Way is of great interest for galaxy formation and evolution processes because of its close proximity enabling studies of individual stars, and because of the likely ubiquity of such systems in the universe. Since their discovery the nature of the thousands of X-ray sources around Sgr A* has long been the subject of extensive investigations beginning with Muno et al. (2003). Direct identification of the X-ray sources in the Galactic Center (GC) region through followup optical/infrared imaging and spectroscopy has been difficult because of severe obscuration

($A_V > 25$), faint counterparts at large distances (~8 kpc), and source crowding (e.g., van den Berg et al. 2009). At a minimum, therefore, a huge investment of time on large telescopes with adaptive optics is required to overcome some of these challenges. Nonetheless, high mass X-ray binaries (HMXBs) were ruled out for a majority early on (Laycock et al. 2005): the lack of bright ($K < 15$) near-infrared counterparts, which are expected from Be stars, the most common companions in HMXBs, indicates that less than 5% of the X-ray sources in the GC region are HMXBs (Mauerhan et al. 2010).

A dominant source type of the X-ray sources in the GC region is currently believed to be magnetic cataclysmic variables (MCVs), in particular, intermediate polars (IPs), which fit the observed luminosity range ($L_X \sim 10^{31-33}$ erg s^{-1} in 2–10 keV) and the unusually hard X-ray spectra with equivalent power-law photon indices[27] of $\Gamma_S \sim 1$ in the 2–10 keV band (Muno et al. 2003; Hong et al. 2009). Active binaries (ABs) have been suggested to make a significant contribution (Revnivtsev et al. 2009, 2011), although this has been disputed (Hong 2012). Perez et al. (2015) recently discovered apparent diffuse hard X-ray emission (20–40 keV) in the central 2′ region around Sgr A* using *NuSTAR* observations. Although the exact origin of the hard X-ray emission is not clear, a leading scenario is that it is from an unresolved population of 1000–10,000 IPs with relatively high mass (>0.8 $M_\odot$) white dwarfs (WDs), which explains a hard thermal component ($kT > 35$ keV) observed in the spectra (see also Hailey et al. 2016). MCVs are indeed likely to be a major component of the X-ray source population at the GC, given their higher abundance relative to BH or neutron star (NS) X-ray binaries (XBs), but a large population of quiescent, exotic BH or NS systems cannot be ruled out yet.

To shed light on the nature of the X-ray source population in the GC, we have surveyed the GC region around Sgr A* using *NuSTAR* (Harrison et al. 2013). Mori et al. (2015) present the results from the *NuSTAR* observations of the diffuse hard X-ray emission in the central 0.2 deg^2 region around Sgr A*. In this paper, we report the first survey results and catalog of hard X-ray *point* sources in a 0.6 deg^2 region around Sgr A* and a 0.06 deg^2 region around the Sgr B2 cloud. With an angular resolution of 18″ in Full-Width Half-Maximum (FWHM), *NuSTAR* is the only hard X-ray telescope capable of resolving X-ray point sources in the crowded GC region. For comparison, previous hard X-ray emission above 10 keV in the same region has been resolved into only three separate sources by *INTEGRAL* (Bélanger et al. 2006).

NuSTAR studies of several prominent sources in the GC region are found in the literature or underway: e.g., CXO J174545.5–285828, a likely run-away pulsar, aka the Cannonball by Nynka et al. (2013); 1E 1743.1–2843, a possible NS low mass X-ray binary (LMXB) by Lotti et al. (2015). The *NuSTAR* observations of bright X-ray flares and bursts in the GC region are presented elsewhere: see Mori et al. (2013) for the *NuSTAR* detection of X-ray pulsations from SGR J1745–29, a transient magnetar (see also Kaspi et al. 2014); Barrière et al. (2014) for the Sgr A* flares; Barrière et al. (2015) for Type I X-ray bursts from GRS1741.9–2853, a NS-LMXB; Younes et al. (2015) for an outburst from GRO J1744–28, also known as the Bursting Pulsar.

[27] In this paper, Γ and Γ_S are used to describe the photon index for a power-law model in the broadband (~3–40 keV) and soft (<10 keV) bands, respectively.

NuSTAR studies of a few bright diffuse sources in the GC region are also found in the literature: Zhang et al. (2014) and Nynka et al. (2015) report detailed *NuSTAR* hard X-ray studies of the X-ray filaments Sgr A–E knot and G359.97–0.038, respectively; Krivonos et al. (2014) and Zhang et al. (2015) present the detailed *NuSTAR* analysis results of the diffuse hard X-ray emission from the Arches cluster and the Sgr B2 cloud, respectively. Complementing the survey of the GC region, a similar *NuSTAR* survey was conducted on the Norma sprial arm region in parallel. Some initial results are reported in Bodaghee et al. (2014), while more complete coverage with an in-depth analysis is underway (A. Fornasini et al. 2016, in preparation).

In Section 2 we review the survey strategies and the *NuSTAR* observations of the GC region and outline the data processing and mosaicking procedures. In Section 3, we introduce a new source search technique: after motivating the need for a new technique (Section 3.1), we demonstrate how to build detection significance maps called "trial maps" based on Poisson statistics-driven random chance probabilities (Section 3.2); we set detection thresholds by cross-correlating the trial maps with a *Chandra* source catalog (Section 3.3) and then present the *NuSTAR* source catalog (Section 3.4). In Section 4, we present the aperture photometry of the *NuSTAR* sources: we describe the aperture selection scheme (Section 4.1) and summarize the photometry results (Section 4.2), followed by the detailed description of spectral classification (Section 4.3), flux and luminosity calculation (Section 4.4), spectral model fitting (Section 4.5) and X-ray variability analysis (Section 4.6). In Section 5, we review the properties of several bright *NuSTAR* sources. In Section 6, we explore unusually hard X-ray sources (Section 6.1) and assess the survey sensitivity (Section 6.2). We address the lack of the foreground *NuSTAR* sources in our survey (Section 6.3) and derive the log$N$–log$S$ distribution of the *NuSTAR* sources (Section 6.4). Finally regarding the nature of the *NuSTAR* sources, we explore two scenarios in addition to NS or BH XBs: MCVs (Section 6.5) and rotationally powered pulsars (Section 6.6).

2. OBSERVATIONS AND DATA PROCESSING

2.1. Observations and Data Screening

Observations of the GC region with *NuSTAR* began in 2012 July, shortly after launch. The original survey strategy for the GC region was to match the central $2^\circ \times 0.^\circ7$ region covered by the *Chandra* X-ray Observatory (Wang et al. 2002; Muno et al. 2009, hereafter M09). The field of views (FOVs) of neighboring *NuSTAR* observations in the survey were designed to overlap with each other by ~40%. Multiple observations of the same region with relatively large FOV offsets tend to average out the vignetting effects of each observation, enabling a more uniform coverage of the region. Multiple observations are also suitable for monitoring long term X-ray variability of sources in the region. Even when observing a single target, the *NuSTAR* observation is often broken up into two or more segments with relatively large pointing offsets to allow an efficient subtraction of a detector coordinate-dependent background component (e.g., Mori et al. 2013).

Our analysis includes three observations of the central Sgr A* field. The observations dedicated to the survey started with a coverage of a 0.2 deg^2 region around Sgr A*, which is called the mini-survey and served as a pilot study. The rest of

the $2^\circ \times 0.^\circ 7$ region was divided into four blocks. It quickly became clear that more than half of the survey region is dominated by stray light (SL) or ghost ray (GR) background from nearby bright sources. SL photons register in the detectors without reflection from the *NuSTAR* optics, arriving from large off-axis angles (~1°–5°) through the open gap between the optics structure and the detector collimators. SL from a bright source forms a circular shaped region of high background in the detectors. GRs arise from photons which only reflect once off the optics ("single-bounce"). A bright GR source generates a set of radial streaks of high background in the detectors. These background components are dominant at low energies, below 10–40 keV, while the internal background becomes dominant above 40 keV; see Wik et al. (2014) and Mori et al. (2015) for more details.

We terminated our survey after coverage of the first two blocks (A and B) because of the severe SL and GR backgrounds expected in the rest of the region. Blocks A and B covered the Galactic northern and western sides of the mini-survey region, respectively. As a result, a continuous $1.^\circ 2 \times 0.^\circ 5$ region around Sgr A* is covered by the survey. In addition, our analysis includes two targeted deep observations of the Sgr B2 cloud. These observations were conducted to measure the hard X-ray emission spectrum from the Sgr B2 cloud and its temporal change in morphology, and they also suffer from severe SL backgrounds. Analysis of the cloud is found in Zhang et al. (2015), and here we report on the X-ray point sources found in the field and their properties.

Table 1 summarizes the *NuSTAR* coverage of the GC region analyzed in this paper. The depths of the various observations are as follows: Sgr A* for 50–160 ks, Sgr B2 for 160 ks, mini survey region for 25 ks, and blocks A and B for 40 ks. We excluded X-ray events in the self-evident SL patterns from our analysis. Table 1 lists the focal plane modules (FPMs) whose SL patterns, if any, were removed. For instance, many observations in block B show bright SL backgrounds in both modules. We also excluded the data when SGR J1745–29 was in outburst (i.e., only three observations of the Sgr A* field were included) and the burst data from GRS 1741.9–2853 (352 s around the peak of the burst from Obs. ID 40010001002), as well as strong and mild flares from Sgr A* (40 ks from Obs. ID 30001002001) in order to improve detection sensitivity of nearby faint point sources (see Table 1).

2.2. Data Processing and Mosaicking

We processed the raw data of each observation to produce event files and exposure maps for both of the *NuSTAR* modules (FPMA and B) using the standard *NuSTAR* pipeline v1.3.1 provided under HEASOFT v6.15.1. The exposure maps used in our analysis, except for non-parametric flux estimations (Sections 4.4 and 6.4), were generated without vignetting effects. For both source detection (Section 3) and aperture photometry (Section 4), we used apertures symmetric with respect to the source position (albeit of different sizes), and thus the vignetting effects are roughly averaged out to first order.

Initially we attempted to localize the positions of a few brightest sources in each observation for astrometric correction of the event files and the exposure maps. This approach did not produce reliable boresight shifts due to relatively high background and lack of bright point sources in individual observations. Instead we use the detection significance map called "trial map" (see Section 3.2), which are generated from the merged image and exposure map (see below) without boresight correction. For the main GC region, we identified 14 bright sources in the trial maps of the 3–10 and 10–40 keV bands with clear *Chandra* counterparts, and localized their positions using the IDL 2D Gaussian fit routine *mpfit2dpeak*. For each observation, the average astrometric shifts of the bright sources in its FOV were used to define the boresight shift for the observation. We assume that there is no offset between the two modules and only translational shifts are needed for astrometric correction (Harp et al. 2010). For five observations with no clear bright sources, we use the original coordinates without any shifts. Table 1 lists the applied boresight shifts and the bright sources used for astrometric correction. Figure 1 shows the distribution of the boresight shifts, which range from $3''$ to $11''$.

The above approach implicitly assumes that the flux of bright sources used for the boresight correction remained constant from observation to observation: or additional iterations are needed to improve the accuracy of astrometric correction. Since the astrometric errors of the final source list based on the inital correction are well within the expected performance of the *NuSTAR* optics ($<5''$ positional errors for the 14 sources used for boresight shifts: see Section 3.4), we did not perform further iterations.

For mosaicking, we re-projected the event files of each observation onto a common tangent point in the sky and merged all of the observations together. We also stacked the data sets of the two modules to maximize photon statistics. We generated a broadband (3–79 keV) image on the common sky grid of the merged event file. For the matching global exposure map, we mosaicked the individual exposure maps by sampling and adding exposure values for every sky pixel in the broadband image. The images mosaicked in this way tend to be free of anomalous changes at the FOV boundaries of the individual observations since it avoids rebinning the different sky grids of the individual exposure maps. We generated a set of the raw count images in six energy bands on the common sky grid: 3–10, 10–40, 40–79, 10–20, 20–40 and 80–120 keV. Since the *NuSTAR* optics have essentially no effective area above 80 keV, the 80–120 keV image is used for a sanity check of the systematic errors. Figure 2 shows an exposure-corrected smoothed *NuSTAR* image in the 10–40 keV band and the vignetting-free exposure mosaic of the main GC region and the Sgr B2 field.

3. SOURCE DETECTION

3.1. Motivation for a New Source Search Technique

Source search routines such as *wavdetect* (Freeman et al. 2002) and *wvdecomp*[28] have been very successful in finding point sources from X-ray images taken by *Chandra*, *XMM-Newton* and other X-ray telescopes. These techniques rely on the correlation between the wavelet kernels and the local count distribution of X-ray images. As researchers lower the detection thresholds of these techniques in hopes of finding fainter sources, it becomes essential to independently validate faint sources detected near the thresholds (e.g., M09; Hong 2012). An independent validation also alleviates a somewhat unavoidable subjectivity inherent in threshold setting (Townsley et al. 2011). In short, negative values used

[28] By A. Vikhlinin; http://hea-www.harvard.edu/RD/zhtools/.

Table 1
NuSTAR Observations of the Galactic Center Region

Observation ID	Pointing (J2000) (1)			Start Time	Exp.	GTI (2)	SL (3)	(4)	Boresight Shift (5)		
	R.A. (°)	Decl. (°)	PA (°)	(UT)	(ks)	(ks)	Removal (FPM)	Total (″)	in R.A. (″)	in Decl. (″)	Reference Source (IDs)
(Sgr A*)											
30001002001	266.4168	−29.0078	333	12-07-20 02:11	167.3	122.1	B	5.89	6.12	−2.45	2743, 1568, 2331
02003	266.4168	−29.0078	336	12-08-04 07:56	83.5	80.4	B	5.15	5.15	−2.51	2743, 6090, 1568, 2331
02004	266.4168	−29.0078	343	12-10-16 18:31	53.9	52.4	B	5.89	6.12	−2.45	2743, 1568, 2331
(Mini Survey)											
40010001002	266.3700	−28.9670	343	12-10-13 06:41	25.8	25.7	B	5.15	5.15	−2.51	2743, 6090, 1568, 2331
02001	266.4480	−29.0080	343	12-10-13 19:21	26.3	26.1	B	5.89	6.12	−2.45	2743, 1568, 2331
03001	266.4370	−28.8710	343	12-10-14 09:56	26.0	25.9	B	5.66	5.26	−3.29	2743, 1568
04001	266.5150	−28.9130	343	12-10-15 00:31	25.8	25.8	B	7.38	7.63	−3.14	7757, 2743, 2331
05001	266.5030	−28.7760	343	12-10-15 13:31	28.1	28.1	B	6.39	6.08	−3.53	7757, 7722
06001	266.5820	−28.8170	343	12-10-16 05:41	25.3	25.3	B	9.08	8.24	−5.50	7757
(Block A)											
40031001002	266.2171	−28.9176	332	13-07-31 14:51	44.0	43.8	B	4.14	1.76	−3.84	6090, 4942
02001	266.1197	−28.8654	332	13-08-01 13:21	43.0	42.8	B	5.67	−1.04	−5.60	5436, 4942
03002	266.2767	−28.8324	332	13-08-03 07:31	40.1	39.7	B	3.07	1.80	−2.64	6369, 6090
04001	266.1794	−28.7801	332	13-08-04 06:01	43.3	43.2	B	6.84	−3.31	−6.19	5436
05001	266.3362	−28.7470	332	13-08-05 04:41	43.5	43.5	B	2.86	1.37	−2.59	6369
06002	266.2389	−28.6949	332	14-08-14 04:56	42.9	42.9	B	4.47	−0.97	−4.39	6369, 5436
07001	266.3957	−28.6617	332	14-08-15 03:21	43.2	43.2	B	2.86	1.37	−2.59	6369
08001	266.2984	−28.6096	332	14-08-16 02:01	43.8	43.6	B	…	…	…	…
(Block B)											
40032001002	265.8947	−29.5664	332	13-08-18 08:01	42.7	42.6	AB	4.85	−5.11	1.94	4515
02001	265.7969	−29.5139	332	13-08-19 08:01	42.7	42.8	AB	10.81	−10.84	−5.28	4067
03001	265.6991	−29.4613	332	13-08-20 08:16	42.8	42.6	AB	10.81	−10.84	−5.28	4067
04002	265.9550	−29.4812	332	13-08-28 11:56	24.4	24.1	AB	4.85	−5.11	1.94	4515
05002	265.8572	−29.4288	332	13-08-25 19:16	27.8	27.7	AB	7.16	−7.99	−1.67	4515, 4067
06001	265.7595	−29.3762	332	13-08-29 12:01	30.8	30.6	AB	10.82	−10.84	−5.28	4067
07001	266.0151	−29.3961	332	13-08-30 12:11	33.4	33.4	AB	4.86	−5.11	1.94	4515
08001	265.9174	−29.3437	332	13-08-31 12:31	37.6	37.6	AB	5.70	−4.03	4.48	4517
09002	265.8198	−29.2912	332	13-09-23 23:11	45.1	45.4	AB	6.46	−6.37	3.29	4517, 4219
10001	266.0752	−29.3109	332	13-09-24 23:11	45.7	45.4	B	4.23	−4.10	2.26	5339, 4517
11001	265.9775	−29.2585	332	13-09-25 23:31	45.1	45.0	AB	5.40	−5.65	2.21	5339, 4517, 4219
12002	265.8800	−29.2061	332	13-09-28 00:11	42.2	42.0	AB	6.46	−6.37	3.29	4517, 4219
13002	266.1352	−29.2257	332	13-10-08 12:21	43.3	43.4	AB	3.68	−4.21	0.03	5339
14002	266.0376	−29.1733	332	13-10-11 09:41	47.3	47.0	AB	5.70	−4.03	4.48	4517
15001	265.9401	−29.1209	332	13-10-12 11:31	43.8	43.7	AB	…	…	…	…
16001	266.1951	−29.1404	332	14-08-17 00:31	44.4	44.2	B	…	…	…	…
17002	266.0975	−29.0881	332	14-08-21 22:41	42.7	42.8	B	…	…	…	…
18002	266.0000	−29.0358	332	14-09-15 02:11	44.3	44.4	AB	5.11	1.22	−5.00	4942
19002	266.2548	−29.0551	337	14-09-29 08:21	46.0	46.0	AB	…	…	…	…
20002	266.1573	−29.0029	339	14-10-19 17:21	41.6	41.6	AB	3.33	2.27	−2.67	6090
21001	266.0599	−28.9506	339	14-10-20 14:06	41.7	41.4	B	5.11	1.22	−5.00	4942
(Sgr B2)											
40012018002	266.7771	−28.3631	339	13-10-22 16:56	153.1	152.6	AB	7.39	1.76	−7.23	8008
19001	266.9404	−28.3655	339	13-10-25 22:31	163.5	161.8	AB	7.61	−1.48	−7.50	8943

Notes. (1) Pointing angle. (2) Sum of good time intervals. The data of Sgr A* flares were excluded. (3) Focal plane module (FPM) where stray light background photons from nearby bright sources were removed. (4) Applied boresight shift. (5) Reference *Chandra* sources used for boresight shift: IDs are from M09.

in wavelet analyses, although enabling efficient source detection, introduce in essence a "subtraction" procedure, which can be inadequate in characterizing the detection significance of X-ray sources from non-negative counts following Poisson statistics.

The relative size of the *NuSTAR* FOV to the point-spread function (PSF) is much smaller than those of *Chandra* or *XMM-Newton*. The ratio of the FOV (∼13′) to the Half-Power Diameter (HPD, 58″) and FWHM (18″) of the PSF in *NuSTAR* is only about 13 and 40, respectively, whereas in *Chandra* the ratio exceeds 1000 (FOV ∼ 17.′5 and HPD <1″ at the aimpoint) for near on-axis sources. Each *NuSTAR* observation often misses a large portion of the PSF of many sources. A point source in the mosaicked data often comprises a number of neighboring observations with partial PSF coverage, varying exposures and different vignetting effects. This, combined with relatively large *NuSTAR* backgrounds with complex patterns, further limits the utility of the conventional techniques for source search in the mosaicked *NuSTAR* data. Except for several self-evident bright sources, all other sources detected by the conventional techniques will have to be re-evaluated by an independent measure.

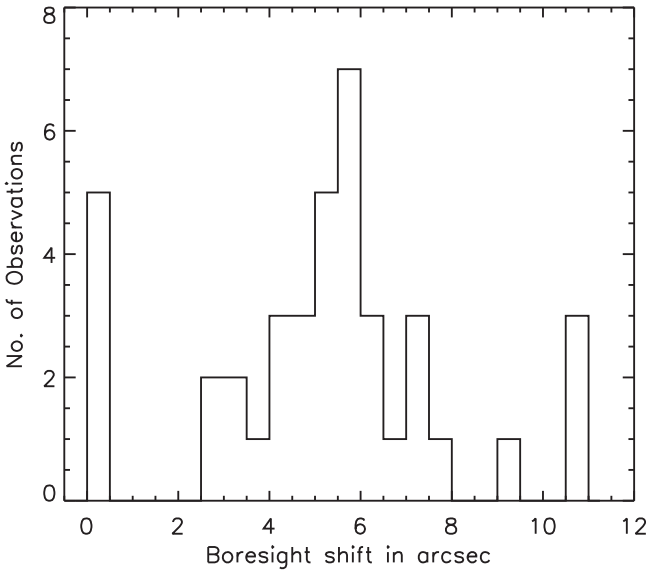

Figure 1. Distribution of the boresight shifts applied for astrometric correction before mosaicking the individual observations. For five observations with no clear bright sources to measure boresight shifts, no astrometric correction is applied. See Section 2.2 and Table 1.

3.2. Trial Maps: New Detection Significance Images

A rigorous probabilistic approach using Poisson statistics is appropriate in describing the significance of source detection in images of positive counts. For a given estimate of background counts, one can calculate the probability of acquiring more than the observed *total* counts solely from a random fluctuation of the background. This probability provides, in fact, a direct indicator of how likely or unlikely it is to have a new source. One of the key aspects of this probabilistic approach is in avoiding subtraction used for handling the background. Weisskopf et al. (2007) and Kashyap et al. (2010) independently calculated this probability (P), which is described by a normalized incomplete gamma function (γ) of the total observed counts and the background estimate:

$$P(N > N^*|\lambda_S = 0,\ \lambda_B) = \sum_{N=N^*+1}^{\infty} \frac{e^{-\lambda_B}\lambda_B^N}{\Gamma(N^*+1)} = \frac{\gamma(N^*+1,\ \lambda_B)}{\Gamma(N^*+1)} = \frac{1}{\Gamma(N^*+1)}\int_0^{\lambda_B} e^{-t}t^{N^*}\,dt \quad (1)$$

where N^* is the observed total counts, λ_B the expected mean background counts, and λ_S the expected mean source counts. The condition, $\lambda_S = 0$, ensures that the probability is calculated for a random fluctuation from the background counts without any source. M09 employed Equation (1) to validate faint sources detected by *wavdetect* and *wvdecomp*.

Our new source search technique uses the above random fluctuation probability as a basis for source detection without relying on other search tools: we calculate P at every sky pixel in the mosaicked images. For a given sky pixel, we first define a source detection cell using a circular region around the pixel and a background cell using a surrounding annulus. Then we estimate λ_B from the counts in the background cell scaled by the ratio of the exposure sum of the pixels in the source and background cells. N^* is simply the total counts in the source cell. Then one can calculate the random chance probability at the sky pixel using Equation (1). We repeat the procedure for every pixel in the image to create a map of the random chance probabilities.

We generate the random chance probability map using three fixed size source cells with radii of 8.″5, 11.″1 and 17.″0 (corresponding to 10%, 20% and 30% enclosures of the PSFs, respectively) in seven energy bands (3–79, 3–10, 10–40, 40–79, 10–20, 20–40 and 80–120 keV). The inner radii of the corresponding background cells are 40″, 51″ and 51″ (60%, 70% and 70% of the PSFs), respectively and the outer radii are set to be 5/3 inner radii.[29] Larger cells enable detections of faint sources in a region relatively free of nearby X-ray emission, while smaller cells enable detections of bright sources embedded in a region of bright X-ray emission.

Unlike the X-ray images taken by *Chandra*, where both the size and shape of the PSFs change significantly across the FOV as a function of the off-axis and roll angles, in *NuSTAR* the size of the PSF remains more or less constant although the shape varies to some extent with the off-axis and roll angles (Madsen et al. 2015). This justifies using fixed-size source and background cells across the field for source search in the mosaicked *NuSTAR* images. In fact, even if the PSF size varies, using fixed-size cells simply means that the resulting probability map retains the features of the PSF shape. In principle, using position-dependent, precise PSFs for source cells allows deconvolution of the PSFs from the image through iterations with forward modeling of the emission geometries. The procedure can be applied to event lists instead of images. If an event list carries the sub-pixel information (e.g., enabled by dithering), using the event list can improve source localization or identification of small structures in the emission geometry. On the other hand, using fixed-size cells on images enables a rapid calculation of random chance probability maps through fast Fourier transformations (FFTs). In this paper, we calculate the probability maps using raw count images instead of event lists and leave applications of varying PSFs on the event lists for future studies. See Appendix A.1 for the resolving power of the *NuSTAR* optics and trial maps using fixed-size cells and Appendix A.2 for diffuse emission structures in trial maps.

Since the random chance probability (P) is opposite to the probability of having a source (i.e., $1 - P$), in order to mimic the usual sense of sky images (i.e., larger values for brighter sources with higher significance), we use the inverse of the random chance probability, which represents the number of random trials needed to produce the observed counts by purely random fluctuations of the background counts. We call the inverse of the random probability maps "trial" maps. Figure 3 shows example trial maps generated in the 3–10 and 10–40 keV bands using 20% PSF enclosures for source cells. The colors are scaled with the logarithmic values (X) of the required random trial numbers (10^X) and the maximum value of the images is limited at $X = 32$ to make the faint sources stand out more clearly.

[29] This choice is made to allow the background cells to be large enough for high photon statistics but not too far off the source cells. Note that source search using multiple scales makes the outcome robust and insensitive to a particular set of the radius selection.

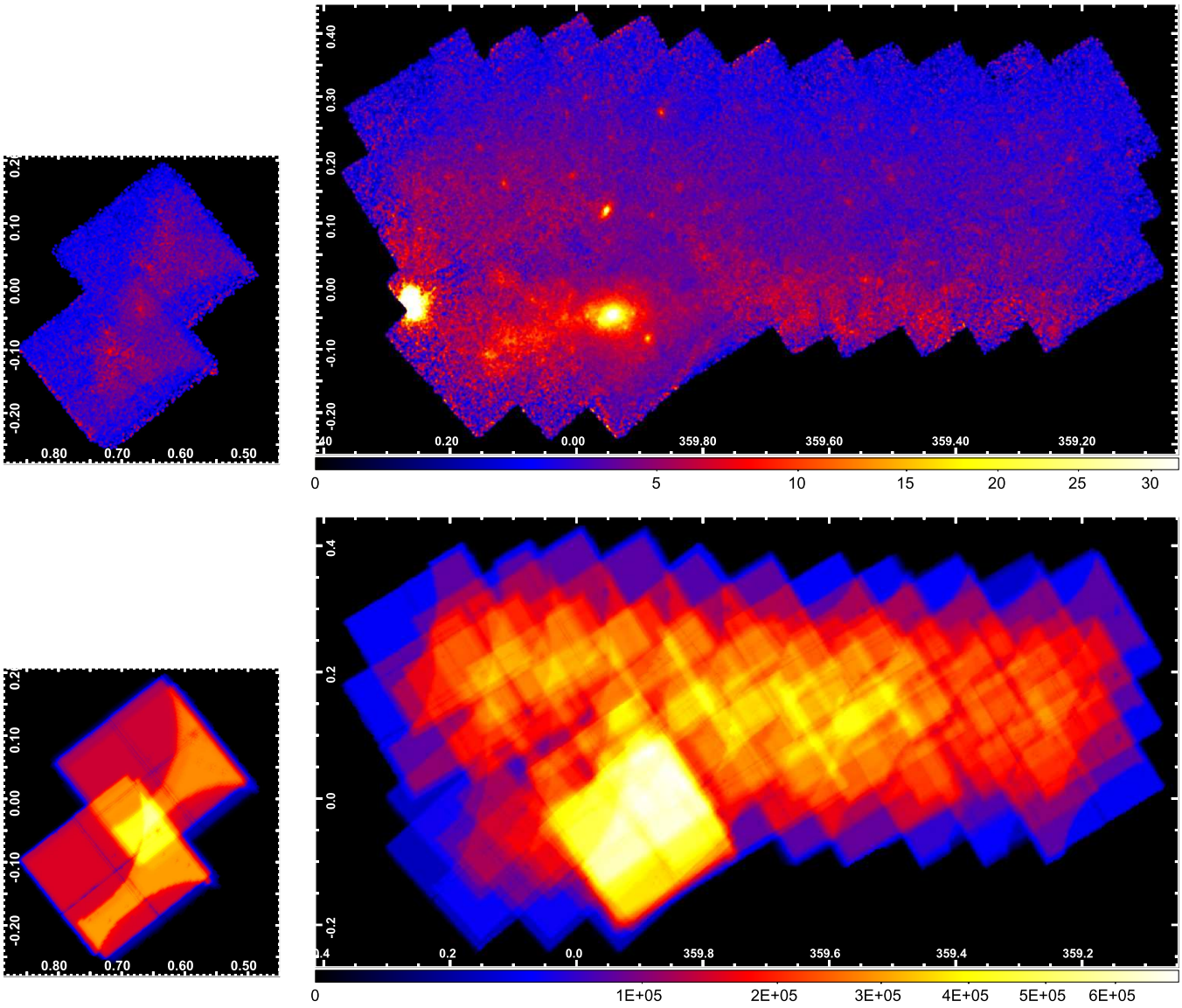

Figure 2. (Top) Exposure-corrected smoothed *NuSTAR* images of the main GC region (right) and the Sgr B2 cloud field (left) in the 10–40 keV band. Smoothing is done via a Gaussian kernel of a four pixel radius in SAOImage DS9. (Bottom) Vignetting-free exposure mosaic of the same regions (not smoothed). The x and y axes are Galactic longitude and latitude, respectively. The color scale of the smoothed image is in counts s^{-1} pix^{-1}, and the exposure map in seconds.

3.3. Threshold Setting for Trial Maps

Trial maps provide the statistical significance of potential sources, but the systematic errors need to be taken into account in order to set a proper detection threshold and thus efficiently detect real X-ray sources while minimizing false detections. Figure 4 shows the cumulative fractional distributions of the random trial numbers with source cells of 20% PSF enclosures in various energy bands. The distribution in the 80–120 keV band, where the *NuSTAR* optics has no response to incoming X-rays, is consistent with an ideal case of purely Poisson statistics-driven random fluctuations of uniform backgrounds (dotted line).[30] The match indirectly indicates that there are no apparent systematic errors in the detector system or in the data processing including the mosaicking procedure. The large excess in the lower energy bands relative to the ideal case originates from the observed celestial sources and the associated systematics of the X-ray optics (e.g., GR backgrounds).

For a given trial map, a statistically conservative detection threshold can be simply the number of pixels ($\sim 5 \times 10^5$ for the main GC region) in the map under the assumptions that each pixel represents an independent search attempt and that one false detection is allowed over the entire map. Since source cells used for search are much larger than a pixel (e.g., 36 pixels in a detection cell of the 15% PSF enclosure), the actual number of independent search attempts in the map is much smaller than the number of pixels. Therefore, the pixel-count based threshold can be a conservative limit for source search in the trial maps of high energy bands (>40 keV) where the statistical errors dominate the systematic errors.

For the trial maps of low energy bands below 40 keV, the pixel-count based threshold is still not stringent enough due to the large systematic errors as seen in Figures 3 and 4. The main cause of the systematic errors in trial maps is the inaccuracy in estimating the true mean background counts (λ_B) in

[30] The cumulative fraction distribution for the ideal background-only case is simply an inverse function of the trial numbers. i.e., 10^{-X}.

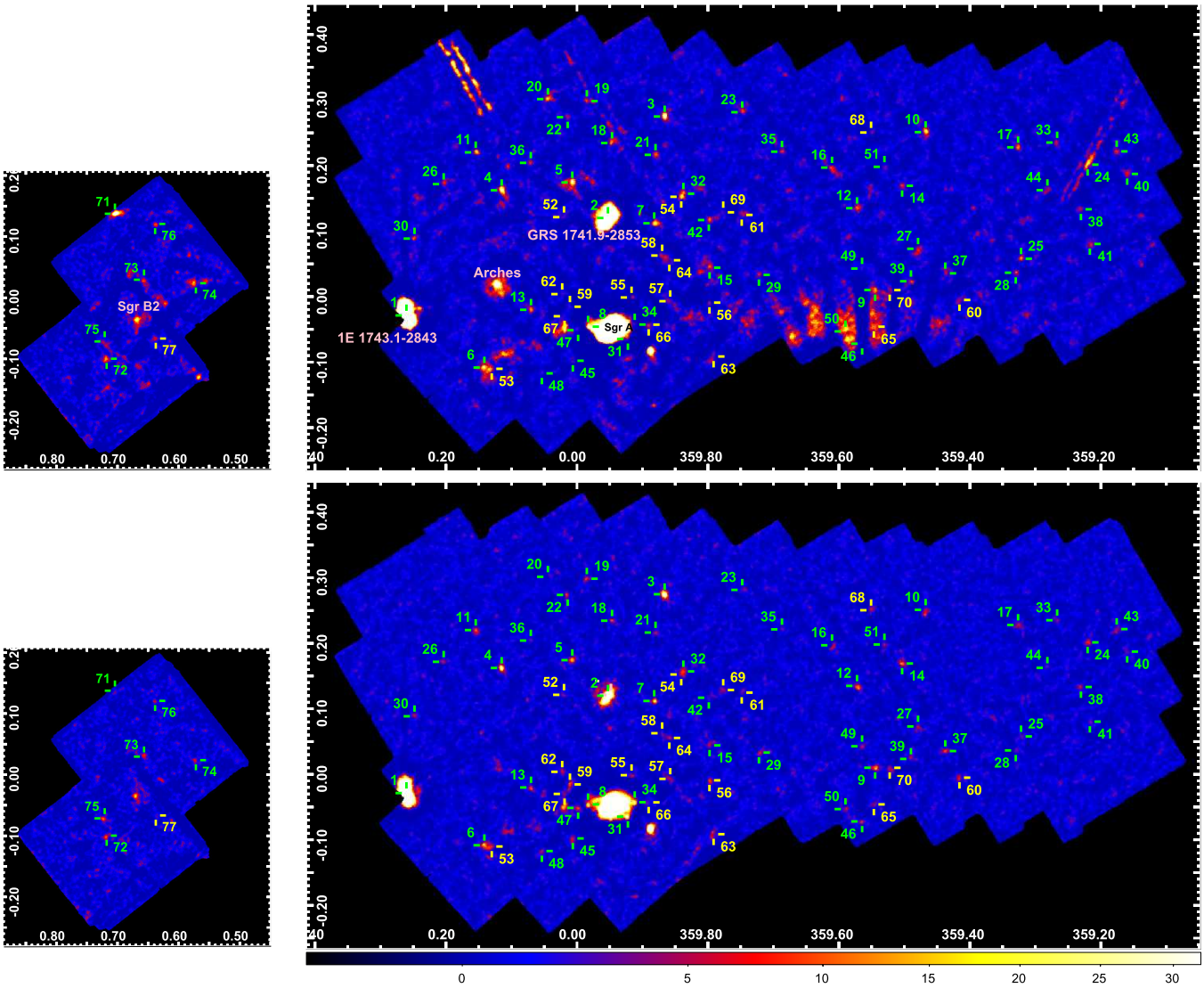

Figure 3. Trial maps of the GC region in the 3–10 (top) and 10–40 keV (bottom) bands using source cells of 20% PSF enclosures, overplotted with the *Chandra* counterparts of the *NuSTAR* detections (green: group 1 and yellow: group 2, Section 3.4). The colors are scaled with the logarithmic values (X) of trial numbers (10^X), and the maximum is set at $X = 32$ to make faint sources stand out more clearly. A few large blobs of high significance include the Sgr A diffuse complex, GRS 1741.9–2853 (Section 5.2), 1E 1743.1–2843 (Section 5.1) and the Arches cluster (Appendix A.2). The large streaks in the 3–10 keV band are (GR) backgrounds from bright sources near the region.

Equation (1). We use the scaled counts of background cells for λ_B, but the background is not uniform. In particular, the contamination from the residual SL and GR backgrounds or large PSF wings of bright neighboring sources does not scale simply by the exposure ratios between the source and background cells. In principle, these systematics can be forward-modeled after initial detections, which would require extensive simulation and modeling work due to the diverse geometries and spectral types of the diffuse and point sources in the GC region. Instead, we evaluate the contribution of the systematics in the trial maps using a deep *Chandra* source catalog by M09 and set proper detection thresholds accordingly.

First, we exclude the regions clearly contaminated by the PSF wings of bright diffuse and point sources. Then, we cross-correlate the remaining region of each trial map with the *Chandra* source catalog. Except for highly variable sources, we expect that the majority of the *NuSTAR* sources have *Chandra* counterparts, so we first search for the *NuSTAR* detection of the *Chandra* sources. Figure 5 shows a scatter plot of the *Chandra* 2–8 keV fluxes of the *Chandra* sources in the GC region M09 and the *NuSTAR* 10–40 keV trial map values at the *Chandra* source positions. For easy illustration, we only show the sources at Galactic latitudes $G_B \geqslant 0.^\circ05$, where no bright diffuse features are observed in the *NuSTAR* 3–79 keV band. Evident is the correlation between the bright *Chandra* sources and their *NuSTAR* trial numbers as highlighted by a green ellipsoid, whereas the sources lying in the gray region at $F_X < 10^{-6}$ ph cm^{-2} s^{-1} in the 2–8 keV band are uncorrelated. For threshold setting, we generate a subset of the trial number distribution using these uncorrelated sources as shown in the shaded histogram on the right panel.

We search for sources in the 18 trial maps (the six energy bands below 80 keV and the three cell sizes). The 18 trial maps are independent of each other in varying degrees. For example, the 3–10 and 10–40 keV trial maps are generated completely independently, while the 3–79 and 10–40 keV trial maps share some common data. We only consider a source as valid in the

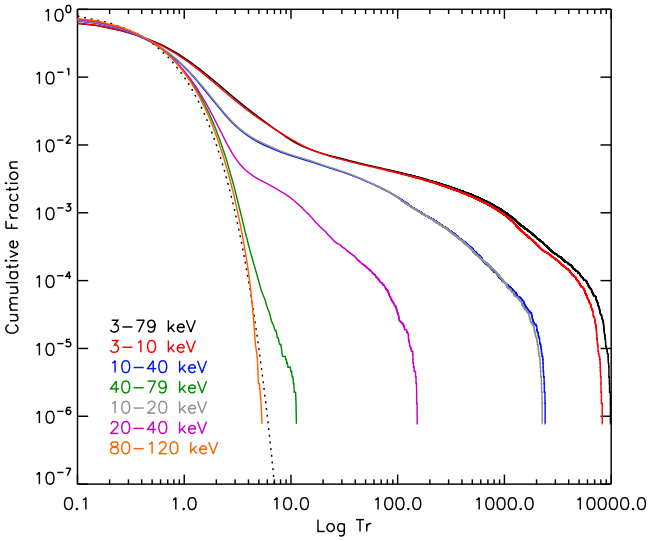

Figure 4. Cumulative fractional distributions of the trial numbers ($\mathrm{Tr} = 10^X$) in various energy bands with source cells of 20% PSF enclosures. Note the x-axis is effectively in a double logarithmic scale (i.e., a logarithmic scale of X). The observed distribution in the 80–120 keV band matches with an ideal case of background-only random fluctuations (the dotted line). In the lower energy bands, the excess relative to the ideal case is due to the observed celestial sources and the associated systematics (e.g., GR backgrounds).

final list if the source is found to be above the threshold in at least two trial maps. For simplicity, we assume that all the trial maps are independent of each other. Then if we require a certain percentage (p) of the false sources to be rejected in each map, the expected false sources (N_F) in the final list is calculated as $N_{\rm can}\, C\,(18,\,2)\, p_{16}\,(1-p)^2$ where $N_{\rm can}$ is the number of *Chandra* sources to consider in search for the *NuSTAR* detection and $C\,(i,\,j)$ is combinatorial or binomial coefficient. To account for some dependency between the maps, we put a tight limit on N_F by setting it at 0.5 instead of 1.

Judging from the correlation pattern in Figure 5, we search the *NuSTAR* detection of the *Chandra* sources only with $F_X \geqslant 3 \times 10^{-6}$ ph cm^{-2} s^{-1} in 2–8 keV. In the main GC region, we have $N_{\rm can} = 264$, and the required rejection percentage (p) for $N_F = 0.5$ is 99.64%. The corresponding thresholds range from $10^{2.7}$ in 40–79 keV with source cells of 15% PSF enclosures to $10^{10.2}$ in the 3–79 keV with 30% PSF enclosures. We also use $N_{\rm can} = N_{\rm pix}$ to calculate a conservative lower limit of the thresholds common for all the maps, which is $10^{4.1}$.

For initial screening, we consider all the sources above the thresholds (regardless of their positions, without any exclusion zone[31]) and all the sources with $F_X > 3 \times 10^{-6}$ ph cm^{-2} s^{-1} in 2–8 keV (regardless of their *NuSTAR* trial numbers). They add up to 290 sources in the main GC region. We visually inspect these 290 candidates in the 18 trial maps and their position in the 18 scatter plots similar to Figure 5. The number of the initial candidates is large because of many *Chandra* sources located in the large diffuse complex near Sgr A*. In the final list we exclude the sources in bright diffuse structures if they are not clearly resolved.

The sources in the Sgr B2 region were selected from their own set of the thresholds by the same procedure. In order to minimize false detections arising from the bright SL background in the Sgr B2 field, we repeat the procedure with two different SL cuts, and only the detections that are common in both cases are selected as real sources.

We also search for *NuSTAR*-only sources without matches to *Chandra* counterparts or possibly missed detections due to the relatively large positional uncertainty of the *NuSTAR* optics (18″ FWHM). To do so, we look for any spots above the thresholds in more than two trial maps outside of the 10″ radius of the *Chandra* positions of the *NuSTAR* detections. We have found two such sources,[32] NGPs 61 and 68. Given the high density of the *Chandra* source population in the region, both of the detections have a *Chandra* source within the positional uncertainty of the *NuSTAR* optics, which is assigned as a potential counterpart.

3.4. Source Catalog

Tables 2 and 3 show the final source catalog of the main GC region and the Sgr B2 region, respectively. Each table divides the sources into two groups and they are listed in decreasing order of the maximum trial value of the 18 maps. The columns of the tables are as follows.

1. *NuSTAR* Galactic Center Point (NGP) source ID.
2. The local peak location of the trial map within 30″ of the *Chandra* position. They are weighted average values among the trial maps with detections. For sources with bright neighbors, we limit the search radius to 10″ or 15″ depending on the proximity. The peak position is determined by a 2D Gaussian fit on the trial map.
3. (Candidate) *Chandra* counterpart ID by M09.
4. (Candidate) *Chandra* counterpart name.
5. The *Chandra* 2–8 keV flux of the counterpart.
6. The angular offset between the *NuSTAR* and *Chandra* positions.
7. The combined exposure of the two *NuSTAR* FPMs at the *Chandra* source positions.
8. An indicator of the soft (S, $<$10 keV) and/or hard (H, $>$10 keV) band detection.
9. The trial map value at the *Chandra* position. The sources are ordered by this value.
10. The energy band of the trial map with the local peak value.
11. The source cell size of the trial map with the local peak value.
12. The number of trial maps above their respective thresholds at the *Chandra* positions.
13. A known name, nearby *Chandra* source, and/or notable diffuse feature nearby.

The sources in group 1 have a relatively clear *Chandra* counterpart which is usually the only bright ($F_X > 3 \times 10^{-6}$ ph cm^{-2} s^{-1}) *Chandra* source around the *NuSTAR* detection. The sources in group 2 have solid *NuSTAR* detections (except for NGP 65, which is a bit marginal), but their association with the *Chandra* sources is not as clear either because multiple *Chandra* sources of similar fluxes are found within the uncertainty of the *NuSTAR* positions (e.g., NGPs 55 and 56)

[31] The exclusion zone (e.g., the large diffuse complex) was only used for setting the thresholds.

[32] When searching for *Chandra* sources in *NuSTAR* trial maps, the values are sampled *at* the *Chandra* source positions: i.e., these two *Chandra* sources have sub-threshold trial values at their *Chandra* source positions, which is the reason that they were not selected in the original search. This approach was chosen to simplify the search procedure in comparison to an alternative method that allows some positional uncertainty in the original search.

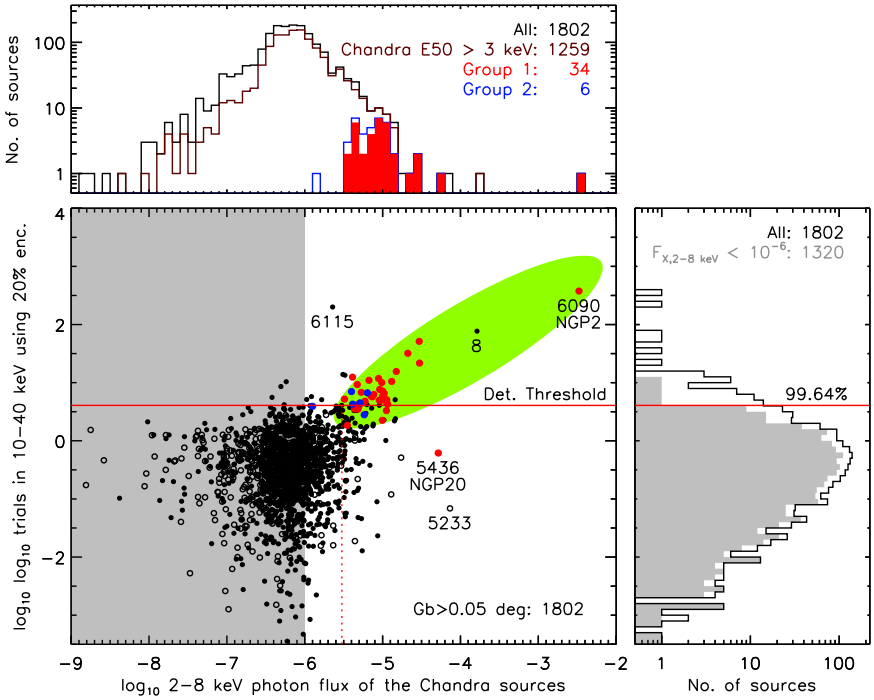

Figure 5. (Left) Scatter plot showing the *NuSTAR* 10–40 keV trial map values vs. the *Chandra* 2–8 keV flux of the 1802 *Chandra* sources at $G_B > 0.^\circ05$ in M09. The sources in the green ellipsoid show a clear correlation, whereas the sources in the gray region at $F_X < 10^{-6}$ ph cm^{-2} s^{-1} are uncorrelated. The open symbols are likely foreground sources (with *Chandra* median energies <3 keV). The *NuSTAR* detections are shown in red and blue for group-1 and 2 sources, respectively (see Section 3.4 for the definition of the source groups). Sources above the threshold (the solid red line) or with a relatively high *Chandra* flux (>3×10^{-6} ph cm^{-2} s^{-1}, the dotted red line) were all visually inspected for detection. (Right) Double logarithmic distributions of the trial map values. The distribution of the sources with $F_X < 10^{-6}$ ph cm^{-2} s^{-1} is used for setting the detection threshold. (Top) Distribution of the *Chandra* 2–8 keV fluxes. *Chandra* source IDs #8 and #6115 are in the bright PSF wings of GRS 1741.9–2853 (see Appendix A.1). *Chandra* ID #5436 (GRO J1744–28) is detected only in the 3–10 and 3–79 keV bands (Section 5.7). *Chandra* ID #5233, which is a foreground star, was not detected by *NuSTAR* (see Section 6.3).

or because a diffuse origin of the hard X-ray emission cannot be ruled out (e.g., NGPs 53 and 59, see Section 6.1). After visual inspection of all the *NuSTAR* detections, we have 58 group-1 and 19 group-2 sources.

Figure 6 illustrates the offset distribution between the *NuSTAR* and *Chandra* positions of the *NuSTAR* detections in the main GC region. The median offset of the distribution is ∼0.″1, and the distribution does not show any significant systematic offsets, validating the astrometric correction of the individual observations. The sources in group 1 show relatively smaller offsets than in group 2, which is in part because group 1 includes the 14 bright sources used for astrometric correction. The maximum offset is 12.″3 for NGP 27. Of five sources with more than 10″ offsets, two sources (NGPs 61 and 68) are found during the search for *NuSTAR*-only detections (Section 3.3); neighboring X-ray emission or nearby artifacts likely contributed to the large offsets of the other three.

4. APERTURE PHOTOMETRY

4.1. Aperture Selection for Photometry

For photometry, we use a circular region and an annulus centered around the *Chandra* position of each source as a basis for source and background apertures, respectively. These apertures are similar to the detection cells used for the source search, but the former are usually chosen to be larger than the latter in order to attain higher photon statistics needed for estimation of various source properties. For example, detection cells used in *wavdetect* for source search in *Chandra* X-ray images typically start with about 30%–40% PSF enclosure circles (Freeman et al. 2002), whereas apertures for photometry are typically about 80%–95% PSF enclosure circles (Broos et al. 2010).

Using apertures symmetric with respect to the source position tends to be effective in alleviating artifacts in the X-ray optics and detector response and also in eliminating the internal and external background components of low spatial frequencies. For instance, the trial maps (Figure 3) generated with the symmetric detection cells lack the large scale diffuse emission that is evident in the (smoothed) raw images (Figure 2).

We use two baseline sets of aperture sizes to assess the systematic errors intrinsic to aperture selection. The first set uses 30″ radius circles (∼50% PSF enclosures) for source apertures and annuli of 50″–80″ radii for the matching background apertures. The second set uses 40″ radius circles (∼60% PSF enclosures) for source and 60″–90″ annuli for background. The baseline apertures work well for relatively isolated sources (about 65%: e.g., top panel in Figure 7), judging from the fact that the estimates of the absorbed photon fluxes in the 3–10 keV band are consistent[33] with the reported 2–8 keV *Chandra* fluxes in M09 within 3σ.

[33] Note that there is a small calibration discrepancy (about 15% level) between the *Chandra* and *NuSTAR* responses (Madsen et al. 2015). In addition, depending on the source spectrum, the difference of the two energy ranges will introduce a small difference in the flux estimate (e.g., about 14% for an absorbed power-law model with $\Gamma = 1$ and $N_H = 6 \times 10^{22}$ cm^{-2}). However, these differences are at the level of the 1σ error of the *NuSTAR* flux estimate except for the first two brightest sources.

Table 2
NuSTAR Galactic Point (NGP) Source List

(1)	(2)		(3)	(4)	(5)	(6)	(7)	(8)	(9)	(10)	(11)	(12)	(13)
No.	*NuSTAR* Position			*Chandra* Counterpart		Offset	Exp.	Det	No.	Energy	Enc.	No.	Comments
ID (NGP)	R.A. (°, J2000)	Decl.	ID	Name (CXOUGC J)	Flux (cgs)	(″)	(ks)		Trials (10^X)	Band (keV)	Size (%)	Det.	
Group 1													
1	266.58731	−28.72770	7722	174621.0–284342	7330.0	3.7	26	SH	14186.0	3–79	30	15	1E 1743.1–2843
2	266.26047	−28.91413	6090	174502.3–285449	3330.0	2.1	301	SH	6881.1	3–10	30	15	GRS 1741.9–2853
3	266.05738	−28.90679	4942	174413.7–285423	29.5	0.4	208	SH	89.4	3–79	30	15	
4	266.31498	−28.75351	6369	174515.6–284512	21.1	1.0	264	SH	74.2	3–79	30	15	
5	266.23912	−28.83940	5972	174457.4–285021	15.0	1.3	268	SH	54.4	3–79	30	12	XMM J174457–2850.3
6	266.59469	−28.87296	7757	174622.7–285218	35.2	4.4	121	SH	45.1	3–79	30	12	an IP, 41″ off #7732 (0.2x)
7	266.22501	−28.97968	5908	174454.1–285842	29.8	4.8	336	SH	44.5	3–79	30	12	
8	266.43964	−28.97497	2743	174545.5–285828	17.2	1.4	468	SH	36.4	3–79	15	12	Cannonball
9	266.12369	−29.31915	5339	174429.5–291909	11.2	2.1	182	SH	32.3	3–79	30	12	on GR
10	265.84154	−29.25912	4219	174321.9–291530	7.4	1.7	183	SH	30.2	3–10	30	10	
11	266.28209	−28.69071	6209	174507.8–284121	9.8	5.0	257	SH	27.6	3–79	30	12	
12	266.01813	−29.23169	4778	174404.2–291349	4.7	5.2	410	SH	25.9	3–79	30	12	
13	266.46651	−28.88695	7113	174551.9–285311	19.7	0.9	181	SH	22.3	3–79	20	12	
14	265.94301	−29.27084	4517	174346.3–291615	4.1	0.8	384	SH	21.8	3–79	30	13	
15	266.23896	−29.08547	5982	174457.8–290509	10.4	7.1	207	S	21.5	3–79	30	5	in a diffuse complex
16	265.98206	−29.16776	4633	174355.2–290955	4.8	10.7	312	SH	21.0	3–79	30	5	large offset, on a streak?
17	265.77970	−29.39092	4119	174306.9–292327	9.9	2.5	187	SH	19.3	3–79	30	9	
18	266.14339	−28.85945	5468	174434.6–285133	13.1	3.9	329	SH	18.8	3–79	30	12	near a streak
19	266.10532	−28.79316	5196	174425.2–284735	10.0	0.1	186	SH	18.7	3–79	30	12	near a streak
20	266.13776	−28.74104	5436	174433.0–284427	51.9	0.4	151	S	18.3	3–10	20	5	GRO 1744–28
21	266.12221	−28.92635	5331	174429.4–285531	10.5	3.2	249	SH	18.0	3–79	30	10	
22	266.14741	−28.78034	5480	174435.2–284651	7.7	3.6	266	H	17.4	3–79	30	6	
23	265.97777	−29.00449	4631	174355.1–290015	9.9	6.9	198	SH	16.9	3–79	30	5	
24	265.74032	−29.49501	4067	174257.7–292942	8.9	1.4	191	SH	16.6	10–20	30	12	on a streak
25	265.94234	−29.48385	4515	174346.2–292902	11.6	0.9	194	S	15.9	3–79	30	6	
26	266.35670	−28.67301	6549	174526.1–284022	9.2	6.6	201	SH	15.5	3–79	30	9	
27	266.02530	−29.34419	4789	174405.3–292031	7.1	12.3	237	SH	15.0	3–79	30	7	near GR
28	265.96794	−29.48868	4590	174352.3–292917	6.2	1.3	183	SH	14.7	3–79	20	7	
29	266.20595	−29.15655	5800	174449.6–290921	6.9	3.4	285	SH	14.7	3–79	20	10	
30	266.46558	−28.67793	7111	174551.8–284041	4.4	2.2	80	S	14.6	3–79	20	6	
31	266.42262	−29.03568	2331	174541.2–290210	7.7	3.4	592	H	14.3	10–40	15	10	near the Sgr A* complex
32	266.15494	−28.99309	5529	174437.1–285934	6.7	1.2	355	SH	13.7	10–20	20	12	20″ off #5559 (1.0x)
33	265.73702	−29.43745	4059	174256.5–292616	5.9	4.0	227	H	13.5	3–79	20	5	
34	266.39373	−29.03403	1568	174534.5–290201	7.4	1.8	569	H	13.0	10–40	15	9	near the Sgr A* complex
35	266.00197	−29.08803	4716	174400.5–290514	9.5	2.0	278	SH	12.4	3–79	30	6	
36	266.24823	−28.76900	6021	174459.5–284610	4.7	1.8	292	S	12.3	3–79	30	5	
37	266.03286	−29.39711	4850	174408.1–292349	5.4	3.2	232	H	11.8	10–40	30	8	
38	265.81460	−29.52082	4159	174315.2–293120	3.2	6.4	229	SH	11.8	3–79	30	7	
39	266.07732	−29.35906	5031	174418.5–292131	7.7	0.9	183	SH	11.7	3–79	30	4	on GR
40	265.71767	−29.55351	4037	174252.3–293314	11.3	2.1	116	S	11.6	3–10	30	4	
41	265.85717	−29.56250	4249	174325.5–293341	9.1	3.0	195	H	11.2	3–79	30	3	
42	266.17014	−29.04797	5600	174441.0–290249	11.2	4.4	255	S	10.4	3–79	20	4	
43	265.69577	−29.52226	4010	174246.5–293119	5.0	5.3	164	S	9.5	3–10	20	4	
44	265.81601	−29.46307	4167	174315.7–292747	3.5	1.3	274	S	9.3	3–10	30	2	
45	266.50491	−28.98072	3627	174601.0–285854	5.8	4.2	239	H	9.2	10–20	30	5	near the Sgr A* complex
46	266.21623	−29.34447	5835	174451.6–292042	2690.0	4.3	85	H	9.0	10–40	20	6	KS 1741–293, near GR
47	266.45443	−28.96449	3022	174548.9–285751	8.7	1.5	466	H	8.7	10–40	20	5	near the Sgr A* complex
48	266.55110	−28.95118	7580	174612.2–285704	3.6	0.7	142	H	8.3	10–20	15	4	near the Sgr A* complex

Table 2
(Continued)

(1)	(2)		(3)	(4)		(5)	(6)	(7)	(8)	(9)	(10)	(11)	(12)	(13)
No.	*NuSTAR* Position		*Chandra* Counterpart				Offset	Exp.	Det	No. Trials	Energy Band	Enc. Size	No. Det.	Comments
ID (NGP)	R.A. (°, J2000)	Decl.	ID	Name (CXOUGC J)	Flux (cgs)		(″)	(ks)		(10^X)	(keV)	(%)		
49	266.10297	−29.28506	5179	174424.7–291706	7.9		0.4	249	H	8.1	10–20	20	4	
50	266.21019	−29.31403	5819	174450.8–291849	9.7		5.7	129	SH	7.9	10–40	20	2	on GR
51	265.93135	−29.23268	4469	174343.4–291358	5.3		1.6	282	H	7.8	10–20	20	4	
52	266.29883	−28.85633	6298	174511.6–285120	11.3		1.4	215	H	7.6	10–20	20	4	detection only with small cells
Group 2 (Unclear Association)														
53	266.59263	−28.88025	7732	174621.5–285256	6.9		11.6	121	SH	37.0	3–79	30	12	#7757 (41″, 5.1x)
54	266.16050	−28.99325	5559	174438.7–285933	6.4		4.1	356	SH	25.6	3–79	20	11	#5529 (20″, 1.0x)
55	266.35586	−29.00918	706	174525.5–290028	5.6		4.9	624	SH	14.4	3–79	15	6	#676 (8.″4, 0.5x)
56	266.29371	−29.11458	6269	174510.3–290649	8.3		3.8	576	SH	13.0	3–79	15	9	#100 (3.″5, 0.4x)
57	266.32800	−29.06134	321	174518.4–290341	0.4		3.3	651	H	13.0	3–79	30	2	#338 (7.″8, 0.8x)
58	266.26736	−29.01466	6131	174504.0–290053	5.1		3.4	621	S	12.8	3–79	30	2	#29 (18.″7, 0.1x)
59	266.42584	−28.93547	2446	174542.3–285606	1.8		2.5	401	H	12.2	10–40	30	7	G0.007–0.014?
60	266.06209	−29.43648	4967	174414.5–292612	3.6		5.0	144	H	11.7	3–79	30	2	4.″7 off 4962, 2x in *Chandra* flux
61	266.12991	−29.08653	5416	174432.1–290508	5.8		10.9	368	SH	11.4	3–79	30	0	*NuSTAR* only
62	266.41357	−28.91540	2138	174539.5–285453	1.4		4.0	270	H	10.5	10–40	30	2	no clear counterpart, low *Chandra* flux
63	266.37198	−29.16144	6592	174528.7–290942	13.3		6.9	316	H	10.4	10–20	30	3	#6603 (7.″3, 0.6x)
64	266.26597	−29.02757	6129	174503.9–290138	4.0		2.5	663	H	10.1	10–40	20	2	on a diffuse streak?
65	266.17681	−29.34647	5649	174442.9–292048	7.8		7.0	85	SH	9.6	10–20	30	1	on GR, marginal
66	266.38364	−29.05174	1219	174531.5–290306	1.9		6.6	560	S	9.3	3–79	20	3	#1332 (14.″2, 1.6x)
67	266.44719	−28.93570	2866	174546.9–285608	0.3		5.2	405	H	9.0	10–40	30	2	low *Chandra* flux
68	265.88886	−29.18793	4343	174334.0–291117	4.1		10.1	246	H	8.4	10–40	30	1	*NuSTAR* only
69	266.14695	−29.05859	5475	174435.0–290334	1.3		4.0	364	H	7.0	10–20	15	2	
70	266.11110	−29.33777	5230	174426.3–292017	2.0		4.4	150	SH	6.7	10–20	20	3	on GR

Note. See Section 3.4 for the column definitions.

Table 3
NuSTAR Point Sources in the Sgr B2 Field

(1)	(2)		(3)	(4)		(5)	(6)	(7)	(8)	(9)	(10)	(11)	(12)	(13)
No.	*NuSTAR* Position		*Chandra* Counterpart				Offset	Exp.	Det	No. Trials	Energy Band	Enc. Size	No. Det.	Comments
4-6ID (NGP)	R.A. (°, J2000)	Dec	ID	Name (CXOUGC J)	Flux (cgs)		(″)	(ks)		(10^X)	(keV)	(%)		
Group 1														
71	266.68683	−28.26511	8095	174645.2–281547	68.4		8.6	85	SH	73.4	3–10	30	7	⋯
72	266.92700	−28.37488	8943	174742.4–282227	13.6		3.3	134	SH	31.7	3–79	30	12	⋯
73	266.76484	−28.35974	8392	174703.5–282136	3.8		2.2	141	SH	24.1	3–79	30	12	⋯
74	266.72262	−28.43308	8209	174652.9–282607	6.0		9.7	277	SH	23.7	3–79	30	10	⋯
75	266.90372	−28.35944	8917	174736.3–282125	4.9		4.2	151	H	17.3	3–79	30	9	⋯
76	266.66580	−28.32988	8008	174639.8–281941	11.6		6.5	142	SH	16.0	3–79	30	10	⋯
Group 2 (Unclear Association)														
77	266.84711	−28.42724	8790	174723.3–282534	3.4		3.8	437	SH	7.1	3–79	20	3	28.″5 off 8815 (1.6x)

Note. See Section 3.4 for the column definitions.

The remaining sources with bright neighbors require additional care in aperture selection. For these sources, the photometry results are often too sensitive to the size of the background apertures. For instance, for NGPs 31 and 34 that are located near the edge of the diffuse emission complex around Sgr A*, the gradient of the emission structure plays an important role in the photometry results. To make aperture selection more objective and thus aperture photometry more reliable, we assume that the soft X-ray fluxes below 10 keV of these sources have not changed significantly from the *Chandra* fluxes reported by M09. Under this assumption, first we reduce the radius of the source aperture by 10″ to limit the contamination. Then we gradually exclude parts of the background aperture that are somewhat dominated by the X-ray emission of the neighbors while maintaining the symmetry of the aperture shape as much as possible until we

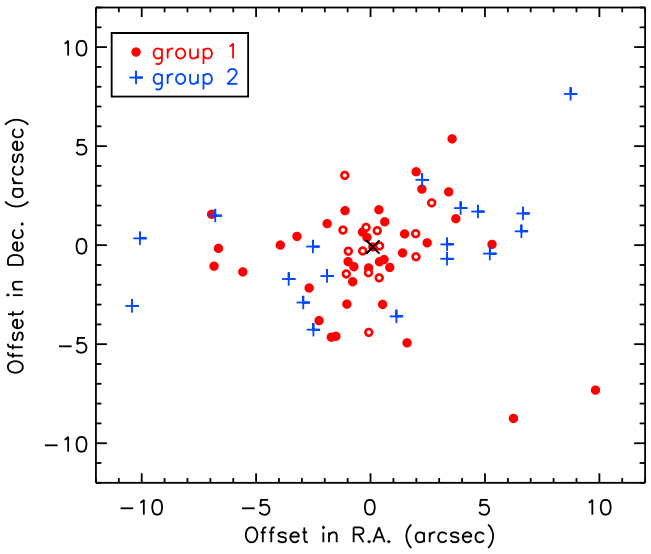

Figure 6. Offset distribution between the *NuSTAR* and *Chandra* positions in the main GC region. The open circles indicate the sources used for astrometric correction. The median offset (~0.″1) of the distribution is marked by an "x" symbol.

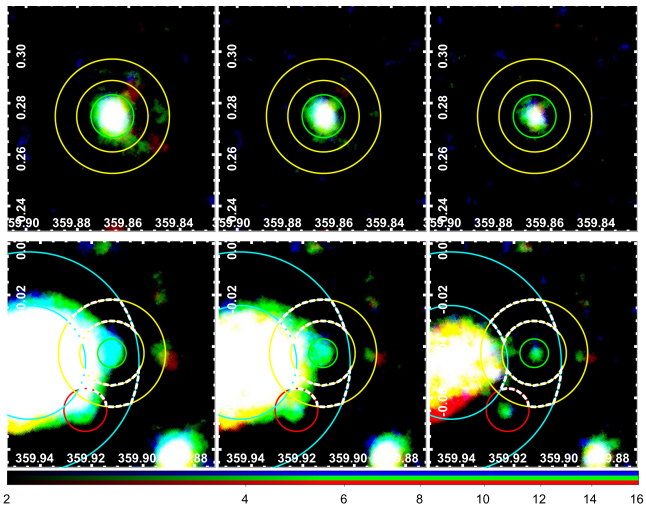

Figure 7. Example aperture selections for photometry overlaid in the trial maps centered around NGP 3 (top) and NGP 34 (bottom). From left to right, the trial maps from 30%, 20% and 15% PSF enclosures for source cells are shown to illustrate the scales of the source and surrounding diffuse emission relative to the aperture selections. In the case of NGP 34, the intersection of the two annuli (yellow and cyan) excluding the neighboring source (red) is used for the background aperture (the dashed lines). The colors are scaled with the logarithmic values (X) of trial numbers (10^X).

get an agreement in photon fluxes between the *NuSTAR* 3–10 keV and *Chandra* 2–8 keV bands within a factor of few.[34]

Figure 7 shows an example aperture selection of NGP 34. We exclude the emission from the Sgr A diffuse complex in the background annulus (yellow) using another annulus (cyan) centered around Sgr A*: we use the intersection of the two annuli for the background aperture. We also exclude the contribution from the neighbor NGP 31 (red). These modifications, although a bit ad hoc, retain the benefits of having (more or less) symmetric apertures and enable a somewhat consistent scheme in aperture selection for all the sources. For bright sources with large PSF wings (e.g., GRS 1741.9–2853), we extended the source and background apertures accordingly.

4.2. Photometry Results

For each source, we extract the events in the source and background apertures from the merged event file and calculate the net counts for a set of energy bands. The relative scale between the source and background apertures is given by the ratio of the summed exposure values (no-vignetting) of the two apertures. Tables 4 and 5 list the photometry results. The columns are defined below and the next few sections describe how we estimate some of the source properties in the table.

1. *NuSTAR* Galactic Center Point (NGP) source ID.
2. *Chandra* source ID by M09.
3. The net counts in the 3–40 keV band.
4. The mode of the posterior distribution of Bayesian Enhanced X-ray Hardness Ratio (BEHR: Park et al. 2006, see Section 4.3): $(H-S)/(H+S)$ where H and S are net counts in 3–10 and 10–40 keV, respectively.
5. The median energy of the *NuSTAR* spectrum in 3–40 keV.
6. A relative ratio of 25% and 75% quartiles: 3 (E_{25}–3 keV)/(E_{75}–3 keV), equivalent to the y-axis value in the *NuSTAR* quantile diagram (Hong et al. 2004, see Section 4.3).
7. An estimate of $N_{\rm H}$ along the line of sight (Nishiyama et al. 2008).
8. An estimate of photon index using the median energy for an absorbed power-law model with $N_{\rm H} = 6 \times 10^{22}$ cm^{-2} (Section 4.3).
9. The observed (i.e., absorbed[35]) *Chandra* 2–8 keV flux from M09.
10. The observed *NuSTAR* 3–10 keV flux (Section 4.4).
11. The observed *NuSTAR* 10–40 keV flux (Section 4.4).
12. The observed *NuSTAR* 3–10 keV luminosity at 8 kpc (Section 4.4).
13. The observed *NuSTAR* 10–40 keV luminosity at 8 kpc (Section 4.4).
14. The source and background aperture radii. (a) 20″/35″–42″, (b) 20″/30″–46″, (c) 20″/45″–75″, (d) 30″/45″–45″, (e) 30″/50″–80″, (f) 40″/60″–90″, (g) 8″/130″–145″, (h) 70″/145″–145″, (i) 70″/210″–230″, (j) 100″/210″–230″. We performed aperture photometry using two aperture sets for each source: the first set to provide the basic photometry results, and the second set to estimate the systematic errors originating from the aperture selection (Section 4.1). The two baseline choices are (e) and (f). An underline indicates the aperture has additional exclusion zones (see Section 4.1).
15. The *NuSTAR* flags: (f) sources showing the iron lines (Section 4.5); (k) sources with short-term variability according to a Kolmogorov–Smirnov (KS) test of individual observations (Section 4.6); (r) sources with long-term variablility according to the maximum-to-minimum flux ratio of multiple observations (Section 4.6). The *Chandra* source flags (M09): (c) sources confused with another nearby source; (g) sources that fell near the

[34] It is not unusual to observe a flux variation by a factor of few from a faint source with a constant luminosity when the observed photon statistics are poor. See Section 4.6.

[35] X-ray photon fluxes and luminosities quoted in this paper are all absorbed quantities using the assumed or estimated $N_{\rm H}$ values unless otherwise noted.

Table 4
NuSTAR Aperture Photometry Results of *NuSTAR* Sources

(1) No.	(2) ID	(3) Net Counts 3–40 keV	(4) Hardness Ratio	(5) Median E_{50} (keV)	(6) Quartile Ratio QR	(7) $N_{\rm H}$ (10^{22} cm^{-2})	(8) Photon Index	(9) F_X (10^{-6} ph s^{-1} cm^{-2}) *Chandra* 2–8 keV	(10) F_X (10^{-6} ph s^{-1} cm^{-2}) *NuSTAR* 3–10 keV	(11) F_X (10^{-6} ph s^{-1} cm^{-2}) *NuSTAR* 10–40 keV	(12) L_X (10^{32} erg s^{-1}) *NuSTAR* 3–10 keV	(13) L_X (10^{32} erg s^{-1}) *NuSTAR* 10–40 keV	(14) Ap. Size IDs	(15) Flag
Group 1														
1	7722	59020(248)	−0.5775(42)	7.152(31)*	1.1707(48)	5.0	1.88(22)†	7330.0	18700(2898)*	6810(940)*	12800(1993)*	15800(2187)*	ij	lscp
2	6090	4134(66)	−0.785(25)*	6.12(11)*	1.123(38)*	7.3	2.63(33)†	3330.0	960 (179)*	118(13)*	610(113)*	245(26)*	gh	krtlscp
3	4942	876 (49)	−0.022(58)	9.84(48)	0.850(72)	3.6	0.84(15)	29.5	28.5(2.4)	50.6(3.7)	21.9(1.8)	139(10)	ef	flg
4	6369	1025(63)	−0.279(71)	8.22(34)	0.918(87)	4.2	1.44(19)	21.1	28.4(2.2)	24.4(2.4)	20.5(1.6)	60.7(5.9)	ef	fr
5	5972	900 (64)	−0.425(63)	7.39(26)	0.86(11)	4.6	1.79(22)	15.0	32.5(6.4)*	17.8(2.4)	22.5(4.4)*	42.0(5.6)	ef	tgc
6	7757	498 (38)	−0.318(71)	7.96(51)	0.96(10)	5.4	1.56(23)	35.2	46(12)*	33.7(4.2)	32.5(8.6)*	82 (10)	cd	fc
7	5908	820 (65)	−0.362(70)	8.07(41)	1.02(14)	4.9	1.46(20)	29.8	24.8(2.4)	18.1(2.5)	17.9(1.7)	44.9(6.3)	ef	rl
8	2743	982 (91)	−0.30(10)	7.44(45)	0.874(97)*	5.5	1.80(22)	17.2	19.7(2.5)	14.2(1.8)	13.7(1.7)	33.4(4.3)	cd	gc
9	5339	524 (58)	−0.05(11)	9.40(79)	1.14(16)	6.5	1.05(27)	11.2	17.1(3.0)	24.4(3.2)	12.9(2.2)	64.6(8.5)	ef	c
10	4219	414 (39)	−0.34(10)*	7.63(48)*	1.13(13)	4.4	1.71(21)	7.4	15.9(3.5)*	10.3(1.8)	11.1(2.4)*	24.7(4.3)	ef	…
11	6209	503 (53)	−0.10(11)	9.03(76)	0.739(86)	3.3	1.12(28)†	9.8	12.5(3.2)*	16.8(4.7)*	9.3(2.4)*	44 (12)*	ef	c
12	4778	737 (66)	−0.25(10)	8.52(58)	0.98(11)	4.2	1.32(23)	4.7	12.4(1.4)	12.1(1.6)	9.1(1.1)	30.7(4.2)	ef	…
13	7113	506 (61)	−0.32(13)	8.25(74)	1.14(21)*	5.2	1.43(31)†	19.7	21.0(3.2)	16.9(3.8)*	15.2(2.3)	42.2(9.5)*	ef	fgc
14	4517	498 (61)	0.10(14)	11.1(1.1)	0.99(16)	4.3	0.52(28)	4.1	6.6(1.4)	15.9(2.2)	5.3(1.1)	45.7(6.5)	ef	…
15	5982	419 (57)	−0.51(15)	7.04(47)	1.11(24)	5.0	1.98(28)	10.4	17.7(4.9)*	7.8(2.3)	12.1(3.3)*	17.9(5.2)	ef	c
16	4633	397 (54)	−0.34(17)	8.03(57)	0.87(22)	3.4	1.52(25)	4.8	9.7(1.6)	7.4(1.7)	6.9(1.2)	18.1(4.2)	ef	l
17	4119	284 (38)	−0.16(16)	8.6(1.2)*	0.96(13)	4.1	1.33(36)†	9.9	10.7(1.9)	11.2(5.3)*	7.8(1.4)	29 (13)*	ef	…
18	5468	554 (59)	−0.41(10)	7.60(52)	1.26(14)	3.7	1.69(25)	13.1	15.6(2.3)*	8.8(1.9)	10.9(1.6)*	21.1(4.6)	ef	g
19	5196	292 (43)	−0.26(18)	8.70(84)	0.82(21)	3.7	1.24(33)	10.0	12.2(2.2)	11.4(2.8)	9.0(1.7)	29.3(7.1)	ef	…
20	5436	297 (39)	−1.00(18)*	5.52(46)	0.73(13)	4.2	3.10(52)	51.9	29.6(3.5)	2.5(2.2)	17.8(2.1)	4.9(4.3)	ef	tlsc
21	5331	369 (50)	−0.46(14)*	7.96(50)	1.15(27)*	4.9	1.51(22)†	10.5	12.5(1.9)	7.0(2.4)*	8.9(1.3)	17.3(5.9)*	ef	…
22	5480	177 (49)	−0.02(31)	9.2(2.0)	1.01(28)	5.5	1.09(80)†	7.7	4.0(1.7)	6.4(2.5)*	3.0(1.3)	16.8(6.5)*	ef	…
23	4631	273 (42)	−0.48(19)	7.12(80)	1.03(21)	3.8	1.91(49)†	9.9	12.4(2.8)*	6.6(2.2)*	8.5(1.9)*	15.2(5.1)*	ef	…
24	4067	465 (43)	−0.44(11)	7.52(53)	1.12(13)	4.3	1.74(26)	8.9	18.4(5.2)*	10.6(1.9)	12.9(3.6)*	25.2(4.6)	ef	c
25	4515	343 (46)	−0.30(16)	7.0(1.8)*	0.86(14)	5.5	1.96(69)	11.6	14.3(3.8)*	10.8(2.3)	9.7(2.6)*	24.9(5.4)	ef	…
26	6549	288 (51)	−0.45(21)	8.08(92)	1.15(27)	3.5	1.52(41)	9.2	9.8(2.1)	6.0(2.0)	7.0(1.5)	14.9(5.0)	ef	c
27	4789	391 (52)	−0.40(15)	8.39(37)	1.49(24)	4.7	1.37(19)	7.1	13.1(2.2)*	8.0(2.1)	9.5(1.6)*	20.1(5.4)	ef	gc
28	4590	219 (45)	−0.38(23)	7.81(86)	1.22(23)	5.4	1.61(41)	6.2	10.6(2.8)*	6.7(2.6)	7.5(2.0)*	16.4(6.3)	ef	lc
29	5800	408 (63)	−0.42(15)*	7.00(65)	1.04(29)	4.9	2.00(41)	6.9	13.0(2.6)*	6.7(2.0)	8.8(1.7)*	15.2(4.5)	ef	…
30	7111	214 (35)	−0.35(21)	8.63(86)	1.19(24)	3.9	1.33(34)	4.4	14.8(3.1)	12.2(3.2)	10.8(2.3)	31.1(8.1)	ef	c
31	2331	1031(112)	−0.06(13)	9.68(91)*	0.96(12)	4.9	1.00(28)	7.7	11.2(2.0)	16.1(1.9)	8.5(1.5)	43.0(5.0)	cd	fg
32	5529	549 (55)	−0.14(13)*	8.31(79)	0.72(11)	4.9	1.39(33)†	6.7	10.9(8.9)*	12.7(3.1)*	7.9(6.5)*	31.9(7.8)*	e	c
33	4059	202 (42)	−0.29(30)	8.5(1.4)*	1.24(25)	4.3	1.35(44)	5.9	5.6(2.8)*	5.8(1.9)	4.1(2.0)*	14.6(4.7)	ef	c
34	1568	886 (97)	0.19(13)	11.00(63)*	1.17(14)	6.3	0.65(16)	7.4	7.3(3.2)*	18.7(1.9)	5.7(2.5)*	52.7(5.2)	cd	f
35	4716	214 (49)	−0.55(32)*	6.5(1.8)*	1.29(55)	3.4	2.25(69)†	9.5	8.4(2.4)*	2.8(2.8)*	5.6(1.6)*	6.3(6.2)*	ef	…
36	6021	275 (58)	−0.68(32)*	6.72(78)	1.33(38)	4.9	2.15(56)	4.7	9.4(2.2)*	2.6(1.7)	6.3(1.5)*	5.9(3.7)	ef	c
37	4850	367 (51)	−0.08(17)*	9.8(1.2)*	0.75(26)	6.0	0.90(27)	5.4	10.0(5.3)*	15.2(2.7)	7.6(4.1)*	41.2(7.3)	ef	c
38	4159	259 (43)	−0.16(17)	9.1(1.1)*	0.94(27)	5.8	1.13(39)	3.2	7.7(2.4)*	9.3(2.2)	5.7(1.8)*	24.4(5.8)	ef	c
39	5031	253 (49)	−0.34(21)	7.2(1.0)	1.04(26)	5.2	1.90(64)†	7.7	10.2(2.6)	7.1(4.5)*	7.0(1.8)	17 (11)*	ef	c
40	4037	190 (28)	−0.38(16)	7.49(65)	1.06(36)	3.6	1.68(35)	11.3	16.0(2.8)	11.2(3.2)	11.3(1.9)	26.9(7.7)	ef	…
41	4249	327 (42)	−0.46(13)	7.53(43)	1.01(23)	4.9	1.73(21)	9.1	13.6(2.0)	7.0(2.0)	9.5(1.4)	16.7(4.7)	ef	…
42	5600	391 (55)	−0.50(13)	7.28(57)	0.98(33)*	4.2	1.84(31)	11.2	13.7(2.1)	6.3(1.9)	9.5(1.5)	14.7(4.5)	ef	…
43	4010	262 (35)	−0.20(14)	7.4(1.0)	0.57(19)	4.1	1.71(61)†	5.0	12.6(2.2)	12.3(2.5)*	8.9(1.5)	29.3(6.1)*	ef	…
44	4167	307 (49)	−0.53(17)	8.04(60)	1.33(37)	4.4	1.52(26)	3.5	9.8(2.1)*	4.4(1.8)	7.0(1.5)*	10.9(4.3)	ef	bc

Table 4
(Continued)

(1) No.	(2) ID	(3) Net Counts 3–40 keV	(4) Hardness Ratio	(5) Median E_{50} (keV)	(6) Quartile Ratio QR	(7) $N_{\rm H}$ (10^{22} cm^{-2})	(8) Photon Index	(9) F_X (10^{-6} ph s^{-1} cm^{-2}) *Chandra* 2–8 keV	(10) F_X (10^{-6} ph s^{-1} cm^{-2}) *NuSTAR* 3–10 keV	(11) F_X (10^{-6} ph s^{-1} cm^{-2}) *NuSTAR* 10–40 keV	(12) L_X (10^{32} erg s^{-1}) *NuSTAR* 3–10 keV	(13) L_X (10^{32} erg s^{-1}) *NuSTAR* 10–40 keV	(14) Ap. Size IDs	(15) Flag
45	3627	282 (45)	−0.02(17)	8.0(3.6)*	0.78(19)	5.5	1.52(96)	5.8	13.0(6.9)*	18.4(3.3)	9.3(4.9)*	45.4(8.0)	cd	f
46	5835	324 (41)	−0.27(13)	8.15(64)	1.18(15)	5.2	1.43(27)	2690.0	39.6(6.6)	35.7(6.8)	28.6(4.7)	89 (17)	ef	tlsp
47	3022	607 (74)	−0.29(14)	8.12(65)	0.89(13)	5.5	1.49(28)	8.7	12.6(2.1)*	10.4(1.8)	9.1(1.5)*	25.8(4.6)	cd	fc
48	7580	210 (53)	0.19(33)	11.6(2.5)	0.63(34)	5.6	0.43(67)	3.6	6.0(3.5)	21.4(4.7)	4.8(2.8)	62 (14)	ef	flc
49	5179	234 (53)	0.17(28)	10.25(91)	1.15(38)	5.7	0.78(28)	7.9	3.6(1.5)	8.7(2.0)	2.8(1.2)	24.1(5.6)	ef	⋯
50	5819	377 (62)	−0.70(15)	7.23(46)*	1.63(22)	5.1	1.84(22)	9.7	42 (30)*	12.0(4.9)	29 (21)*	28 (12)	ef	c
51	4469	212 (47)	0.05(95)*	10.7(4.8)*	0.69(28)*	3.5	0.63(76)	5.3	3.8(3.0)*	8.3(2.2)	3.0(2.4)*	23.5(6.2)	ef	l
52	6298	251 (54)	−0.04(28)	9.2(1.7)	1.01(25)	5.7	1.06(65)†	11.3	8.9(2.9)	12.7(3.9)*	6.7(2.2)	34 (10)*	ef	c
Group 2 (Unclear Association)														
53	7732	194 (47)	−0.26(25)	8.4(1.5)	0.67(26)	5.1	1.38(66)	6.9	16.9(5.5)	15.5(5.3)	12.2(4.0)	39 (13)	ab	c
54	5559	447 (56)	−0.47(14)*	7.11(53)	1.03(17)	4.7	1.93(31)†	6.4	12.3(6.3)*	5.4(6.4)*	8.4(4.3)*	13 (15)*	e e	lc
55	706	470 (83)	−0.05(29)*	9.9(2.8)*	1.05(19)	5.6	0.88(36)	5.6	5.1(8.3)*	8.4(1.6)	3.9(6.4)*	23.0(4.3)	c d	fc
56	6269	488 (91)	0.16(28)*	10.6(1.2)	1.13(46)*	4.5	0.63(34)	8.3	6.7(5.8)*	15.4(3.0)	5.2(4.6)*	43.3(8.5)	ef	fc
57	321	589 (97)	−0.19(19)*	8.0(1.0)	1.04(21)	5.0	1.51(50)	0.4	5.7(3.2)*	6.1(1.3)	4.1(2.3)*	15.1(3.3)	ef	c
58	6131	446 (84)	−0.59(21)*	6.05(65)	0.47(33)*	4.4	2.59(60)†	5.1	9.6(1.9)	2.9(2.1)*	6.1(1.2)	6.1(4.3)*	ef	c
59	2446	443 (87)	0.49(51)*	13.8(3.7)*	1.29(49)*	5.0	0.01(21)†	1.8	2.7(3.8)*	19.4(4.3)*	2.3(3.2)*	60 (13)*	ef	⋯
60	4967	358 (46)	−0.16(12)	8.63(99)	0.93(19)	5.6	1.27(40)	3.6	20.7(3.7)	23.3(4.1)	15.2(2.7)	60 (10)	ef	c
61	5416	335 (63)	−0.59(22)	7.52(71)	1.44(36)	3.4	1.72(37)	5.8	9.0(1.8)	3.7(1.7)	6.3(1.3)	8.8(4.1)	ef	⋯
62	2138	389 (67)	−0.01(19)	9.6(1.4)	0.73(12)*	5.6	0.92(49)	1.4	8.8(2.5)	14.8(2.9)	6.7(1.9)	40.0(8.0)	ef	flg
63	6592	420 (61)	0.02(24)*	10.3(1.8)*	0.88(20)	6.3	0.69(36)†	13.3	11.5(4.7)*	25.7(4.2)*	9.0(3.7)*	72 (12)*	ef	c
64	6129	659 (88)	−0.39(13)	7.45(68)*	0.91(36)*	4.6	1.73(33)	4.0	10.2(3.0)*	6.1(1.5)	7.1(2.1)*	14.5(3.6)	ef	fgc
65	5649	216 (49)	−0.55(23)	7.5(1.1)	1.15(26)	5.5	1.74(63)†	7.8	22.5(6.2)	11.6(6.7)*	15.7(4.3)	28 (16)*	ef	c
66	1219	499 (112)	−0.41(26)	7.72(82)	1.45(28)	6.1	1.68(40)	1.9	6.3(3.1)*	3.4(1.4)	4.4(2.1)*	8.1(3.4)	ef	f
67	2866	533 (96)	−0.07(19)	9.8(1.6)*	0.84(23)	4.9	0.88(29)	0.3	7.5(4.1)*	12.8(2.5)	5.8(3.2)*	34.7(6.9)	ef	c
68	4343	129 (42)	1.00(62)	13.1(3.3)	1.11(80)*	3.7	0.15(74)†	4.1	1.3(1.3)*	8.4(2.9)*	1.1(1.1)*	25.4(8.6)*	ef	⋯
69	5475	340 (63)	0.43(41)*	12.6(2.0)*	0.79(33)	4.2	0.24(37)	1.3	3.2(3.1)*	13.7(2.3)	2.6(2.6)*	40.9(6.9)	ef	⋯
70	5230	263 (47)	−0.27(27)	9.35(96)	0.95(21)	5.8	1.06(34)	2.0	11.4(2.9)	13.1(3.1)	8.5(2.2)	34.8(8.2)	ef	⋯

Note. See Section 4.2 for the column definitions.

Table 5
NuSTAR Aperture Photometry Results of Sources in the Sgr B2 Field

(1)	(2)	(3)	(4)	(5)	(6)	(7)	(8)	(9)	(10)	(11)	(12)	(13)	(14)	(15)
No.	ID	Net Counts 3–40 keV	Hardness Ratio	Median E_{50} (keV)	Quartile Ratio QR	$N_{\rm H}$ (10^{22} cm^{-2})	Photon Index	F_X (10^{-6} ph s^{-1} cm^{-2})			L_X (10^{32} erg s^{-1})		Ap. Size IDs	Flag
								Chandra 2–8 keV	*NuSTAR* 3–10 keV	*NuSTAR* 10–40 keV	*NuSTAR* 3–10 keV	*NuSTAR* 10–40 keV		
Group 1														
71	8095	311(27)	−0.81(19)*	6.561(92)	1.69(14)*	4.8	2.20(28)†	68.4	136(13)*	18.2(9.0)*	90.5(8.9)*	40 (20)*	ef	-:
72	8943	518(48)	−0.335(84)	7.76(55)*	0.88(12)	4.9	1.72(21)	13.6	22.1(4.5)*	13.7(2.2)	15.5(3.1)*	32.7(5.2)	ef	…
73	8392	327(42)	−0.23(14)	8.56(62)	0.78(16)	4.8	1.41(24)	3.8	11.6(2.1)*	9.9(2.0)	8.4(1.5)*	24.9(4.9)	ef	…
74	8209	585(62)	−0.50(11)	7.08(32)	1.00(17)	5.2	1.91(23)†	6.0	19.4(5.5)*	9.0(2.3)*	13.3(3.8)*	20.8(5.2)*	ef	gc
75	8917	360(42)	0.02(15)	9.73(93)*	0.97(12)	5.3	0.98(26)	4.9	9.6(4.5)*	15.0(2.2)	7.3(3.4)*	40.1(5.9)	ef	…
76	8008	162(37)	−0.59(42)*	7.9(1.2)*	1.68(53)	4.6	1.48(25)†	11.6	11.8(3.0)*	6.3(4.1)*	8.5(2.2)*	16 (10)*	ef	c
Group 2 (Unclear Association)														
77	8790	352(70)	−0.66(34)*	6.76(36)	1.73(32)	4.4	2.09(26)	3.4	9.0(1.8)	2.6(1.7)	6.1(1.2)	5.9(3.7)	ef	c

Note. See Section 4.2 for the column definitions.

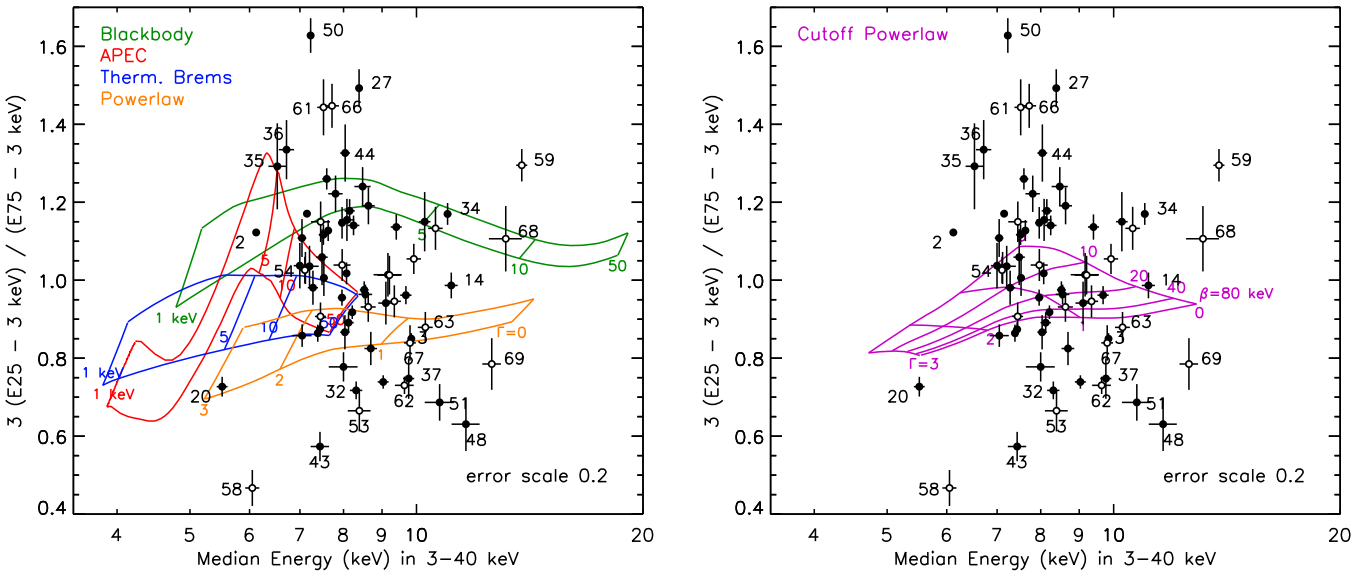

Figure 8. Quantile diagrams of the *NuSTAR* sources in comparison with five spectral models. The grids on the left panel are for absorbed power-law (yellow, from right to left, photon indices of 0, 1, 2, and 3), thermal bremsstrahlung (blue), APEC (red), and blackbody (green) models. The thermal models cover kT of 1, 5, 10 and 50 keV, which run from left to right. The height of the grid pattern in each model represents the variation between $N_{\rm H} = 10^{22}$ and 10^{23} cm^{-2}. The grid on the right panel is for an absorbed cut-off power-law model $[E^{-\Gamma}\exp(-E/\beta)]$ with $N_{\rm H} = 6 \times 10^{22}$ cm^{-2}. The covered photon indices (Γ) are 0, 1, 2 and 3, and the cut-off energies (β) are 5, 10, 20, 40 and 80 keV. The closed and open circles are from the group-1 and 2 sources, respectively. The error bars are scaled down to 20% of the original values for easy viewing.

edge of a detector in one or more observations; (*b*) sources for which the source and background spectra have a >10% chance of being drawn from the same distribution according to the KS tests; (*s*) sources variable on short timescales, as indicated by probabilities of <1% that the event arrival times for at least one observation were consistent with a uniform distribution according to the KS test; (*l*) sources that were variable on long timescales, as indicated by a probability of <1% that the fluxes for all observations were consistent with a uniform distribution according to the KS test. Others: (*t*) transients identified in Degenaar et al. (2012).

The errors quoted in Tables 4 and 5 are the largest of the three estimates: a statistical error and two different estimates of systematic errors. The statistical error is estimated from the uncertainty of the observed net counts after background subtraction. A systematic error is given by the difference in the photometry results between two aperture sets (marked with *). In calculating the photon indices and the X-ray luminosities, another systematic error is estimated based on the selection of spectral model parameters (marked with †, see Section 4.4).

4.3. X-Ray Hardness Ratio and Energy Quantiles

We use the Bayesian Estimation of Hardness Ratios (BEHRs; Park et al. 2006) and the energy quantiles (Hong et al. 2004) to classify the spectral types of the *NuSTAR* sources. Conventional hardness ratios or X-ray colors are often subject to a spectral bias intrinsic to the choice of the energy bands. The BEHRs alleviate the intrinsic spectral bias through a more rigorous probabilistic approach. Energy quantiles are free of such a spectral bias and enable an easy classification of diverse spectral types.

We use the BEHR between the 3–10 and 10–40 keV bands and the median energy in 3–40 keV as an illustrator of the overall spectral hardness. The quoted value of the BEHR is the mode of the posterior distribution of $(H - S)/(H + S)$ where H and S are net counts in 3–10 and 10–40 keV bands, respectively. The error represents the larger deviation of the ±34% range (1σ equivalent) of the posterior distribution. The error of an energy quantile is given by the standard deviation of the quantiles from 100 randomly selected half-sampled sets of the source events.

For a two-parameter classification, X-ray color–color diagrams are often used, but the poor statistics and the diverse spectral types frequently result in only upper or lower limits for many estimates of X-ray colors. We use quantile diagrams consisting of the median energies versus the quartile ratios (see also Section 6.3). Figure 8 shows *NuSTAR* quantile diagrams in 3–40 keV overlaid with several spectral model grids. The grids on the left panel indicate power-law (yellow), thermal bremsstrahlung (blue), APEC (red) and blackbody (green) models with absorptions of $N_{\rm H} = 10^{22}$ and 10^{23} cm^{-2} to guide the spectral type of the *NuSTAR* sources. We use Anders & Grevesse (1989) for the abundance model in the absorption. The power-law model covers $\Gamma = 0$, 1, 2 and 3, and the thermal models cover $kT = 1$, 5, 10 and 50 keVs. The grid on the right panel is for an absorbed cut-off power-law model $[E^{-\Gamma}\exp(-E/\beta)]$ with $N_{\rm H} = 6 \times 10^{22}$ cm^{-2}. The cut-off energies (β) cover 5, 10, 20, 40 and 80 keV, and the photon indices (Γ) range 0, 1, 2, and 3. The error bars are scaled down to 20% of the original values for easy viewing.

The quantile diagram illustrates that the X-ray spectra of some sources (e.g., NGP 2) are better described by thermal plasma models while others (e.g., NGP 3) by non-thermal power-law models, which is not clear from the BEHRs or the median energies alone. Sources that lie in between the blackbody and power-law model grids can be better described by an absorbed cut-off power-law model as seen on the right panel. However, due to the relatively large uncertainties of the quartile ratios and the degeneracy among the different spectral

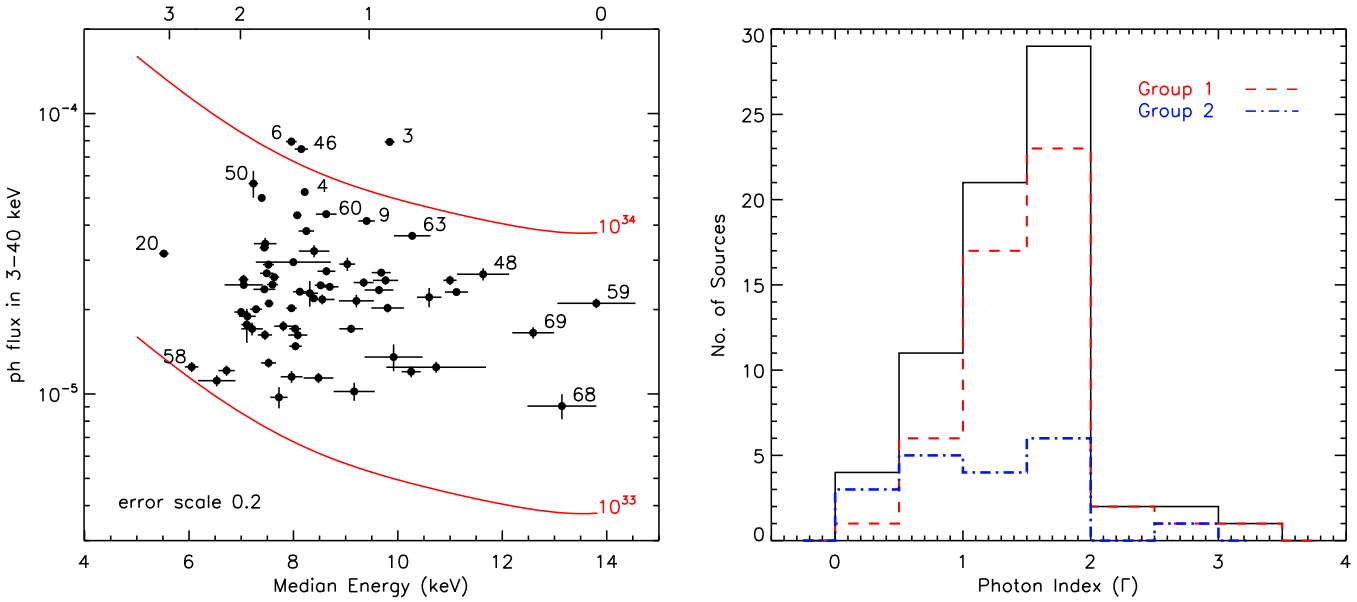

Figure 9. Scatter plot of photon flux vs. median energy of the *NuSTAR* sources (left) and their equivalent photon index distribution (right). The top *x*-axis on the left panel shows the equivalent photon indices for an absorbed power-law model with $N_{\rm H} = 6 \times 10^{22}$ cm^{-2} (Section 4.3). The two lines show the iso-luminosity tracks for $L_X = 10^{33}$ and 10^{34} erg s^{-1} at 8 kpc in the 3–40 keV band. The error bars are scaled down to 20% of the original values for easy viewing. The red, blue and black histograms shows group-1, 2 sources and the sum of the two, respectively.

models in the diagram, it is not straightforward to assign both spectral models and parameters for many sources from the quantile diagram.

4.4. Flux and Luminosity Estimates

To properly account for the spectral type in estimation of observed photon flux and luminosity of each source, we use an absorbed power-law model with the median energy-based photon index. We also assume $N_{\rm H} = 6 \times 10^{22}$ cm^{-2}, which is often used to describe the interstellar absorption for sources in the GC region (e.g., M09). For comparison, Table 4 also lists an estimate along the line of sight toward each source based on the A_{Ks} map of the GC region generated from the observations by the SIRIUS camera on the Infrared Survey Facility telescope (Nishiyama et al. 2008). The resolution of the A_{Ks} map is 15″. Their values range from $N_{\rm H} \sim 3$–7×10^{22} cm^{-2}, whereas the estimates based on the *NuSTAR* quantile diagram (or the X-ray color–color diagrams) are often higher with large uncertainties. Some of the bright sources such as the Cannonball (NGP 8) indeed exhibit an X-ray spectrum with a higher extinction than the field estimate or the assumed value, which may be the result of the local absorption around the source, but the *NuSTAR* X-ray band (>3 keV) is not sensitive to the absorption below $N_{\rm H} \sim 10^{23}$ cm^{-2} (Section 5.6).

To assess the systematic error arising from an inaccurate assumption of the extinction, we re-estimate the photon index by changing the $N_{\rm H}$ value to 3× and 12 $\times 10^{22}$ cm^{-2}. We also re-calculate the photon index by varying the median energy by 1σ with the $N_{\rm H}$ value fixed at 6×10^{22} cm^{-2}. The systematic error is given by the largest difference between the original estimate and these four estimates. This systematic error is quoted with † in Table 4, if it is larger than the statistical error and the difference between the two aperture sets (Section 4.1).

The left panel in Figure 9 shows a scatter plot of absorbed 3–40 keV photon flux versus median energy of the *NuSTAR* sources. The tracks show the iso-luminosity lines for absorbed power-law models with $N_{\rm H} = 6 \times 10^{22}$ cm^{-2}. The top-axis shows the equivalent photon indices. The error bars on the left panel are scaled down to 20% of the original values for easy viewing. The right panel in Figure 9 shows a distribution of equivalent photon index of the *NuSTAR* sources for an absorbed power-law model.

Table 4 shows the observed photon fluxes calculated for an absorbed power-law model with the median energy-based photon index and $N_{\rm H} = 6 \times 10^{22}$ cm^{-2}. We also estimate the photon fluxes non-parametrically (not shown in the table), where we calculate the net counts in every 1 keV step, convert them to the matching photon fluxes by using the Auxiliary Response Function of the source and then summing them over a given energy band. This direct conversion from photon counts to fluxes is not usually encouraged because the conversion is prone to large amplification of statistical noise. On the other hand, the non-parametric estimation offers a sanity check of the model dependence in the flux and luminosity estimations (see Section 6.4). The difference between the model-based and model-independent estimates are less than 40% except for a few of the faintest sources. On average, the non-parametric estimation is about 6%–11% lower than the power-law model-based estimation, depending on the energy bands.

For estimation of observed luminosities, we use an absorbed power-law model and a distance of 8 kpc for all the sources with $N_{\rm H} = 6 \times 10^{22}$ cm^{-2}, assuming they all are in the central Galactic Bulge (Section 6.3). The uncertainty in $N_{\rm H}$ is not a dominant factor of uncertainties in the flux and luminosity estimations. For several brightest sources, we compare the estimates from the spectral model fits with simple median-energy based estimates in Section 5.

4.5. Spectral Model Fit for Bright Sources

For some of the bright *NuSTAR* sources with net counts greater than ~600 (excluding ones already in the literature), the

Table 6
Spectral Model Fit Results of Four Bright *NuSTAR* Sources (see Section 4.5 and Figure 10)

Source ID	NGP 3		NGP 4		NGP 7		NGP 34	
Chandra ID	#4942		#6369		#5908		#1568	
Energy Band (keV)								
NuSTAR	5–26		3–23		3–24		5–26	
XMM-Newton	2.5–10		2–10		2–10		4–10	
Chandra	2–10		2–10		2–10		2–10	
Models	Power-law	APEC	Power-law	APEC	Power-law	APEC	Power-law	APEC
Relative Normalization								
XMM-Newton	$1.7^{+0.4}_{-0.4}$	$1.4^{+0.3}_{-0.3}$	$1.0^{+0.5}_{-0.4}$	$0.9^{+0.4}_{-0.3}$	$1.3^{+0.4}_{-0.3}$	$1.1^{+0.3}_{-0.2}$	$1.8^{+0.5}_{-0.4}$	$1.3^{+0.3}_{-0.2}$
Chandra	$1.3^{+0.3}_{-0.2}$	$1.1^{+0.2}_{-0.2}$	$1.3^{+0.5}_{-0.3}$	$1.1^{+0.3}_{-0.2}$	$1.2^{+0.4}_{-0.3}$	$1.0^{+0.3}_{-0.2}$	$1.1^{+0.4}_{-0.3}$	$1.7^{+0.2}_{-0.1}$
Parameters								
$N_{\rm H}(10^{22}$ cm$^{-2})$	17^{+7}_{-6}	26^{+5}_{-5}	13^{+7}_{-7}	16^{+5}_{-4}	13^{+5}_{-5}	15^{+3}_{-4}	54^{+9}_{-8}	52^{+6}_{-5}
Photon Index	$0.9^{+0.3}_{-0.3}$	…	$1.1^{+0.5}_{-0.5}$	…	$1.2^{+0.4}_{-0.4}$	…	$1.5^{+0.4}_{-0.4}$	…
kT (keV)	…	$64^{+\infty}_{-13}$	…	$64^{+\infty}_{-47}$	…	$22^{+\infty}_{-8}$	…	12^{+5}_{-3}
Abundance	…	1 (f)	…	1 (f)	…	1 (f)	…	$1.4^{+0.7}_{-0.5}$
Fe Kα Energy (keV)	6.4 (f)	6.4 (f)	6.4 (f)	6.4 (f)	…	…	6.4 (f)	$6.37^{+0.04}_{-0.04}$
Fe Kα EW (eV)	770^{+260}_{-240}	580^{+200}_{-190}	620^{+380}_{-300}	600^{+340}_{-290}	…	…	160^{+100}_{-70}	160^{+70}_{-60}
χ^2_r /dof	0.96/54	1.21/54	0.88/21	0.92/21	1.20/47	1.14/48	1.51/104	1.23/102
F_X 3–10 keV (10^{-5} ph cm^{-2} s^{-1})	$2.7^{+0.3}_{-1.0}$	$3.1^{+0.5}_{-2.9}$	$1.9^{+0.2}_{-1.7}$	$2.1^{+0.7}_{-2.0}$	$2.5^{+0.3}_{-2.1}$	$2.8^{+0.4}_{-0.6}$	$0.9^{+0.1}_{-0.9}$	$1.3^{+0.2}_{-0.3}$
F_X 10–40 keV (10^{-5} ph cm^{-2} s^{-1})	$5.0^{+0.5}_{-1.6}$	$3.4^{+0.4}_{-3.4}$	$2.6^{+0.4}_{-2.6}$	$1.9^{+0.5}_{-1.9}$	$3.0^{+0.5}_{-2.3}$	$1.8^{+0.3}_{-0.8}$	$1.6^{+0.2}_{-1.6}$	$0.9^{+0.2}_{-0.2}$
L_X 3–40 keV (10^{33} erg s^{-1})	$15.9^{+1.4}_{-5.3}$	$10.7^{+1.2}_{-10.5}$	$8.3^{+1.4}_{-8.2}$	$6.1^{+1.6}_{-0.1}$	$9.6^{+1.4}_{-6.9}$	$6.0^{+1.0}_{-2.0}$	$4.7^{+0.5}_{-3.8}$	$3.0^{+0.4}_{-0.7}$

spectra were analyzed through spectral model fitting in addition to the spectral classification described in Section 4.3. We also search for the *Chandra* and *XMM-Newton* archival data, and if available, we jointly fit the *NuSTAR* spectra with the *Chandra* and/or *XMM-Newton* spectra. The *Chandra* spectra are from M09. The *XMM-Newton* spectra are from the *XMM-Newton* pipeline processing system. For sources with multiple *XMM-Newton* observations, we regenerate a spectrum of each observation and stack them together to get a combined spectrum.

We generate a combined *NuSTAR* spectrum for each source by stacking individual X-ray spectra from multiple observations with proper scalings using the FTOOL *addspec*. As aforementioned, if a source is covered by multiple observations, it is bound to fall near the edge of a chip in some of them. Those observations that miss a large portion of the PSF are excluded in building the stacked spectrum since their individual spectra are of poor statistics and their instrumental responses are likely subject to a large uncertainty. As a result, the stacked X-ray spectra of many sources do not have sufficient photon counts to put meaningful constraints on the spectral parameters through model fitting. In other words, high detection significance in Table 2 or high net count in Table 4 does not guarantee a *NuSTAR* X-ray spectrum with high signal-to-noise ratio. Out of the nine *NuSTAR* sources with net counts greater 600, Table 6 summarizes the best-fit parameters of four sources with relatively good spectral fits for absorbed power-law and APEC models (Section 5). Note that the *Chandra* and *XMM-Newton* spectra were taken much earlier than the *NuSTAR* observations. The best-fit normalizations relative to *NuSTAR* are listed in Table 6.

We also explored the *Chandra* spectra of the 15 *NuSTAR* sources with >200 net counts in the *Chandra* 0.3–8 keV band to constrain the presence of the iron lines at 6.4 and 6.7 keV. We fit the *Chandra* spectra with and without the iron lines for an absorbed power-law model (Section 6.5). The sources showing the iron lines are flagged with "*f*" in Table 4.

4.6. X-Ray Variability

The millisecond time resolution of the *NuSTAR* FPMs allows us to characterize the timing properties of detected sources over a range of timescales. The *NuSTAR* timing resolution is ~2 ms rms, after corrected for thermal drift of the on-board clock, and the absolute accuracy is known to be better than 3 ms (Mori et al. 2014; Madsen et al. 2015). In our search for periodic modulations (see below), all photon arrival times are converted to barycentric dynamical time (TDB) using the *Chandra* coordinates of each point source.

To characterize the source variability we used the KS statistic to compare the temporal distributions of X-ray events extracted from source and background apertures in the 3–40 keV energy band of each observation. The background lightcurve acts as a model for the expected source counts as a function of time. The maximal difference between two cumulative normalized lightcurves gives the probability that they are drawn from the same distribution. i.e., that the source tracks the background. If the probabilities of the KS statistics are less than $\sim 3.8 \times 10^{-5}$, which is equivalent to 1% random chance probability after taking into account the number of search trials (i.e., the sum of the number of observations searched for each source), we consider the source as variable and it is flagged with "*k*" in Table 4. We manually checked the source and background lightcurve for candidate variable sources to avoid the false detection due to background fluctuation. NGP 2 is the only source showing significant variablility.

Table 7
X-Ray Variability of *NuSTAR* Sources

(1) No. ID (NGP)	(2) *Chandra* ID	(3) F_X in 3–40 keV Mean	(4) Min	(5) Max	(6) Flux Ratio (r) Max/Min	(7) >84.13%	(8) >99.87%	(9) Ran. Prob. (10^{-X}) $f_1 \leqslant$ Min $f_2 \geqslant$ Max	(10) $f_2/f_1 \geqslant r$	(11) No. Obs.	(12) Sep. (days)	(13) Var. Flags
		(10^{-6} ph s^{-1} cm^{-2})										
2	6090	1080(17)	<5.6	3999(65)	>715	⋯	⋯	>30.0	>8.0	3/5	364	kr
3	4942	79.2(4.4)	73(10)	118(11)	1.6	1.4	1.0	6.5	2.0	3/5	446	
4	6369	52.5(3.2)	34.8(5.2)	75.0(9.0)	2.2	1.8	1.2	4.3	3.5	4/4	377	r
5	5972	50.0(3.6)	29.0(8.7)	72.2(6.5)	2.5	1.9	1.2	5.0	2.1	4/5	2	⋯
7	5908	43.4(3.4)	24.2(4.9)	101(12)	4.2	3.4	2.2	17.1	6.3	4/7	806	r
9	5339	41.4(4.6)	49.6(9.9)	65.7(7.4)	1.3	1.1	0.7	5.7	0.7	2/3	14	⋯
17	4119	21.7(2.9)	7 .0(4.8)	39.3(5.9)	5.6	3.2	1.5	5.5	2.1	4/4	25	⋯
19	5196	24.1(3.5)	6 .3(7.7)	51.5(7.9)	8.1	3.3	1.5	6.6	2.0	3/3	2	⋯
20	5436	31.7(4.1)	18.3(7.1)	67(11)	3.7	2.5	1.3	7.5	2.2	3/4	375	⋯
29	5800	19.6(3.0)	8 .3(5.5)	38.8(6.0)	4.7	2.7	1.3	5.7	2.0	4/4	43	⋯
45	3627	29.5(4.7)	<10	83(17)	>8.1	⋯	⋯	>6.6	>2.5	5/8	3	⋯
56	6269	22.1(4.1)	13.0(7.3)	98(12)	7.5	4.7	2.5	>18.0	1.9	5/6	786	⋯
66	1219	9.7(2.2)	3 .7(6.2)	36.9(6.0)	10	3.2	1.4	7.5	1.7	3/6	73	⋯

Note. (3), (4) and (5) The mean, minimum and maximum values of the observed flux in the 3–40 keV band, respectively. (6) The maximum-to-minimum flux ratio (r). (7) and (8) An estimate for the 1 and 3σ equivalent lower limit of r, respectively, without accounting for the multiple searches (67 sources with multiple observations). (9) The random chance probability (X in 10^{-X}) for flux measurements (f_1, f_2) with f_1 being lower than the observed minimum and f_2 being higher than the observed maximum without accounting for the multiple searches (243: the sum of the number of observations for each source). (10) The random chance probability with the ratio (f_2/f_1) being higher than the observed the ratio (r) without accounting for the multiple searches (67 sources). (11) The number of the observations used for flux calculation and the number of the observations with the source in their FOV. The former excludes the observations where the source falls near the chip edge. (12) The time difference between the maximum and minimum flux measurements. (13) Flags for short (k) and long (v) term variability. See Section 4.2.

In the case of variability from observation to observation, in order to account for the large differences in the off-axis responses among multiple observations of a given source, we compare the observed fluxes of each source calculated under the proper response function of each observation and use the maximum-to-minimum flux ratio (r) as an indicator of the variability. Table 7 lists sources with multiple observations that show possible flux variability. A caveat is that the error of the flux ratio is in general dominated by the relatively large uncertainty of the minimum flux value, which often implies r being statistically consistent with 1 (i.e., no variability) even for the cases with $r \gg 1$ (e.g., NGP 66). Columns 7 and 8 in Table 7 show the lower limit of the observed flux ratio equivalent to 1 and 2σ, respectively. Many of these limits are very close to 1 even though these limits do not account for the number of the search trials (67 sources with multiple observations).

In order to evaluate the significance of the observed flux ratios, we calculate two random chance probabilities for each soure under the assumption of the source flux being constant: a probability for observing a higher-than maximum flux and a lower-than minimum flux (column 9) and a probability for having the flux ratio greater than the observed flux ratio (column 10). The probabilities in the table are without accounting for the search trial numbers. The former is more binding and thus less probable than the latter since the former uses specific flux values in calculating the probability, and as a result, it is much more sensitive to the accuracy of the mean flux estimate than the latter. The total number of the search trials in the two are also different: in the former it is proportional to the total number of the searched observations (e.g., $10^{-4.4}$ in column 9 is equivalent to a true random probability of ∼1% after accounting for the trial numbers), whereas in the latter it is proportional to the number of the searched sources (e.g., $10^{-3.8}$ in column 10 is equivalent a true random probability of ∼1%).

Table 7 shows that it is not unusual to observe a high flux ratio (≫1) even for a constant flux source, depending on the photon statistics. The three sources NGP 2 (Section 5.2), 4 (Section 5.4) and 7 (Section 5.5) show very significant flux variations under both scenarios of the random chance probabilities, and they are flagged with r. The observed flux ratios of the other sources appear statistically probable even if their X-ray emission is actually steady, but the large deviation of observed minimum and maximum fluxes relative to the mean values may imply some degree of the flux variation.

We also searched for a pulsar signal from those *NuSTAR* sources with sufficient counts to detect a coherent timing signal, determined as follows. The ability to detect pulsations depends strongly on the source and background counts and number of search trials. For a sinusoidal signal, the aperture counts (source plus background) necessary to detect a signal of pulsed fraction f_p is $N = 2S/f_p^2$, where S is power associated with the single trial false detection probability of a test signal $\wp = e^{-S/2}$ and is distributed as χ^2 with two degrees of freedom. In practice, for a blind search, we need to take into account the number of frequencies tested $N_{\rm trials} = T_{\rm span} f_{\rm Nyq}$, when $T_{\rm span}$ is the data span and $f_{\rm Nyq} = 250$ Hz, the effective *NuSTAR* Nyquist frequency. In computing f_p we must allow for the reduced sensitivity of the search due to background contamination in the source aperture (N_b); the minimum detectable pulse fraction $f_{p,\rm min}$ is then increased by $(N_s + N_b)/N_s$ where N_s is the source counts.

We computed the pulsar signal detectability in individual observations for each source in our sample and find that nearly all sources proved undetectable even if their flux were 100% pulsed. However, we have identified four sources for which we can potentially place a meaningful limit of $f_{p,\rm min} < 50\%$ on the pulsed flux, at the 3σ confidence level. These are the first four

entries in the bright source list below, NGP 1–4. For each source we evaluated the power at each frequency (oversampling by a factor of two) using the unbinned Z_n^2 test statistic (Buccheri et al. 1983) summed over $n = 1$, 2, 3 and 5 harmonics, to be sensitive to both broad and narrow pulse profiles. We initially searched photon arrival times with energies in the 3–40 keV range and used an nominal 30″ aperture. We repeated our search for an additional combination of energy ranges 3–25 keV, 3–10 keV, 10–25 keV, and 10–40 keV, and for aperture sizes of $r < 20''$ and $r < 30''$. For all these searches no significant signal was detected. We found $f_p < 6.1\%$ for NGP 1 from one observation and <8.0% for NGP 2 (the best out of the three observations) at 3σ, and the other two sources (NGPs 3 and 4), where the search was divided into three observations for each source, did not produce a meaningful upper limit on the pulsed fraction.

5. BRIGHT X-RAY SOURCES

In this section, we review the broadband X-ray properties of nine bright *NuSTAR* sources, including four sources for which detailed analyses of the *NuSTAR* observations are found in the literature. We analyze the broadband spectra of four other *NuSTAR* sources using the *Chandra* and *XMM-Newton* archival data, and comment on another bright X-ray source detected by *NuSTAR*.

5.1. NGP 1 (1E 1743.1–2843 or #7722)

1E1743.1–2843 was discovered by the *Einstein Observatory* more than three decades ago (Watson et al. 1981) but the precise nature of the source remains unclear. Lotti et al. (2015) present the results of recent *NuSTAR* and *XMM-Newton* observations of the source. They concluded that between two proposed scenarios, LMXB or HMXB, it is likely a LMXB based on the argument that the absence of periodic pulsations, eclipses or the Fe K_α line in the X-ray emission disfavors the HMXB scenario more strongly. X-ray spectral model fitting requires a composite model, which includes a disk blackbody and a cut-off power-law component. For an absorbed power-law model, the median energy is consistent with $\Gamma = 1.9 \pm 0.2$ and the quantile analysis (see Section 4.3 and Figure 8) favors a thermal plasma model indicating a strong thermal component in the X-ray emission. It was the brightest source in our survey of the GC region with an absorbed photon flux reaching $\sim 2 \times 10^{-2}$ ph cm^{-2} s^{-1} in the 3–40 keV band. Lotti et al. (2015) estimate a luminosity of $L_{2-10\,\mathrm{keV}} \sim 10^{36}$ erg s^{-1} at 8 kpc, which is consistent with our estimate: $L_{3-10\,\mathrm{keV}} \sim 1.3 \pm 0.2 \times 10^{36}$ erg s^{-1} within 2σ.

5.2. NGP 2 (GRS 1741.9–2853 or #6090)

Since its discovery by the *Granat* satellite (Sunyaev 1990), the transient X-ray source GRS 1741.9–2853 (AX J1745.0–2855), has produced at least a dozen Type I outbursts, typical of LMXBs binaries (Cocchi et al. 1999), recorded by several X-ray telescopes over the years (see Degenaar et al. 2014, and references therein for a review). *NuSTAR* observed GRS 1741.9–2853 four times, during one of which a Type I burst was fully recorded. A comprehensive paper on these data sets is presented in Barrière et al. (2015). These authors were able to place a lower limit of 6.3 kpc on the distance to the NS based on the peak flux from the burst assuming the photospheric radius expansion model. They argue that spectral variation during outburst suggests disturbances in the inner accretion disk resulting from the burst. In the work herein we exclude a 352 s burst interval and report our analysis results in Table 4. Table 7 shows a significance flux variation by nearly three orders of magnitude and during a quiescent period the flux fell below the detection level.

We generally reproduce the earlier result. The median energy of the X-ray spectrum is consistent with an absorbed power-law model with $\Gamma = 2.6 \pm 0.3$. The quantile diagram indicates that the overall X-ray spectrum, which is still dominated by the outbursts even after the exclusion of the peak burst period, is more consistent with blackbody emission than a power-law model (Figure 8 in Section 4.3), as expected, since the thermal emission from the surface becomes dominant during the outburst periods. For a timing analysis we considered the quiescent, outburst, and burst intervals separately. The source and background counts combination for each interval allows for a well constrained pulsar search. A comprehensive search did not produce a significant signal for any interval, consistent with the null timing search result reported in Barrière et al. (2015).

5.3. NGP 3 (CXOUGC J174413.7–285423 or #4942)

NGP 3 is a bright, very hard X-ray source in block A with a median energy of ~10 keV. It is one of a few sources that are detected above 20 keV and the 3rd brightest sources in the 10–40 keV band with an X-ray luminosity of 1.4×10^{34} erg s^{-1}. The measured X-ray fluxes of the source appear to vary by 60% between two observations, about 14 months apart, but such a variation in the measurement is statistically plausible even for a constant flux source (i.e., 70% chance to see such a variation from a source when accounting for the search trials, Table 7). Figure 10(a) shows a joint model fit of non-simultaneous *NuSTAR* (black), *Chandra* (red) and *XMM-Newton* (green) spectra for an absorbed power-law model with a Gaussian line fixed at 6.4 keV. The best-fit photon index is 0.9 ± 0.3 and the Gaussian line improves the fit (from $\chi_r^2 = 1.49$–0.96) with the best-fit equivalent width (EW) of 770 eV (Table 6). For single temperature thermal models, the plasma temperature is not well constrained but the best-fit plasma temperature for an absorbed APEC model is $\gtrsim$30 keV with 95% confidence. The 3–40 keV absorbed luminosity at 8 kpc estimated by the spectral fit is $(1.1$–$1.6) \times 10^{34}$ erg s^{-1}, which is consistent with the aperture photometry result, 1.6×10^{34} erg s^{-1}. Given the hard continuum in the X-ray spectrum with the neutral iron line, we suspect that NGP 3 is most likely an IP, although the observed X-ray luminosity at 8 kpc is at the high end of the luminosity distribution for IPs.

5.4. NGP 4 (CXOUGC J174515.6–284512 or #6369)

NGP 4 is another bright X-ray source in block A with a median energy of 8.2 keV. It is also detected in the 20–40 keV band. Four observations covered the source and we excluded one of the module B data due to the SL background. The X-ray flux of NGP 4 varied by about a factor of two over about a year, which has ~3% random chance probability when accounting for the 67 sources searched for the variability (Table 7). Figure 10(b) shows a joint model fit of the *NuSTAR* (black), *Chandra* (red) and *XMM-Newton* (green) spectra for an absorbed power-law model with a Gaussian line fixed at 6.4 keV. The best-fit photon index and EW are 1.1 ± 0.5 and

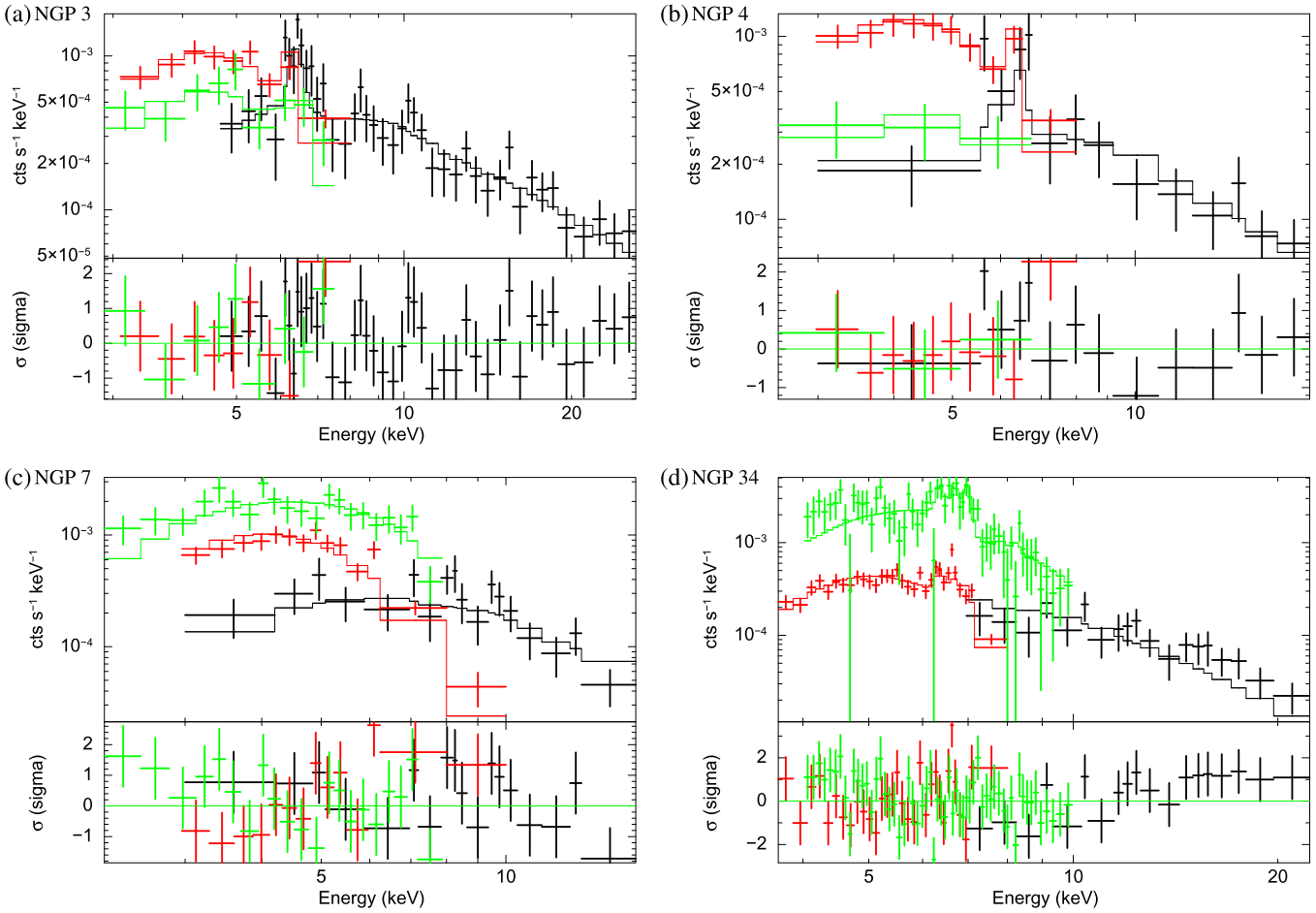

Figure 10. Joint spectral model fits of four bright *NuSTAR* sources: (a) NGP 3 or *Chandra* ID #4942 (see Section 5.3), (b) NGP 4 or #6369 (Section 5.4), (c) NGP 7 or #5908 (Section 5.5), (d) NGP 34 or #1568 (Section 5.8). The *Chandra*, *XMM-Newton* and *NuSTAR* spectra are shown in red, green and black, respectively. The solid lines are the best-fit model for an absorbed power-law model in (a), (b) and (c), and for an absorbed APEC model in (d). The models for (a), (b) and (d) include a 6.4 keV neutral Fe line. See Table 6 for the best-fit parameters.

620 eV, respectively. The spectral model fit requires the Gaussian line, otherwise the reduced χ^2_r increases to 1.5. For thermal plasma models, the spectral fit does not constrain the plasma temperature. The 3–40 keV absorbed luminosity estimated by the spectral fit is (6.1–8.3) $\times$ 10^{33} erg s^{-1}, which is consistent with the aperture photometry estimate, 8.1 $\times$ 10^{33} erg s^{-1}. This source is also suspected to be an IP.

5.5. NGP 7 (CXOUGC J174454.1–285842 or #5908)

NGP 7 is located in the overlapping section of the mini survey, blocks A and B. As a result, seven observations covered the source, but we excluded two observations and the FPM B of another, which did not contribute much. The X-ray flux shows the 2nd largest variation after NGP 2, changing by a factor of four over two years. Constant, steady X-ray emission from the source is statistically ruled out (Table 7). Figure 10(c) shows a joint model fit of non-simultaneous *NuSTAR* (black), *Chandra* (red) and *XMM-Newton* (green) spectra for an absorbed power-law model. The spectral fit does not require any iron lines. The best-fit photon index is 1.2 $\pm$ 0.4. In the case of an absorbed APEC model, the plasma temperature is poorly constrained but the best-fit temperature is significantly lower than NGPs 3 and 4. The 3–40 keV luminosity at 8 kpc estimated by the spectral fit and aperture photometry are 6.0 $-$ 9.6 $\times$ 10^{33} and 6.2 $\times$ 10^{33} erg s^{-1}, respectively. Given the photon index, the lack of the neutral iron line in the X-ray spectrum and the large X-ray variability, we suspect the source is a quiescent NS or BH XB or a background active galactic nucleus (AGN).

5.6. NGP 8 (The Cannonball or #2743)

The Cannonball, discovered by *Chandra* in 2003 (Muno et al. 2003), is likely a run-away pulsar 2′ northeast of Sgr A*, just outside the radio shell of the supernova remnant (Zhao et al. 2013). The cometary emission surrounding the source is interpreted as a pulsar wind nebula (PWN) and the projected velocity is estimated about 500 km s^{-1} (Park et al. 2005; Zhao et al. 2013), but no pulsation has been detected so far. The detailed spectral analysis of the *NuSTAR* observation of the source can be found in Nynka et al. (2013). They observed a non-thermal component up to 30 keV in the X-ray spectrum, which is described by an absorbed power-law model with $\Gamma = 1.6 \pm 0.4$ and $N_{\rm H} = 3.2 \times 10^{23}$ cm^{-2}. Their estimate of the absorption is about 5 times larger than the typical interstellar absorption assumed in the GC region, and also higher than the estimates based on A_{Ks} (Section 4.3). The high extinction is consistent with the idea of the local absorption caused by the surrounding PWN. Our estimate of the photon index ($\Gamma \sim 1.8 \pm 0.2$) under the assumption of $N_{\rm H} = 6 \times 10^{22}$ cm^{-2} still matches theirs within the

uncertainty, reconfirming the presence of the non-thermal emission above 10 keV. The unabsorbed X-ray luminosity in the 2–30 keV band is about 1.3×10^{34} erg s^{-1} according to Nynka et al. (2013). The corresponding observed luminosity in 3–40 keV is about 10^{34} erg s^{-1}, which is consistent with our estimate, $\sim 9 \times 10^{33}$ erg s^{-1}.

Given the complex diffuse emission surrounding the source, the background aperture has to be carefully selected as discussed in Section 4.1. Despite the significant difference in aperture selection between our analysis and Nynka et al. (2013), the consistent results between the two are encouraging and indirectly validate our aperture photometry procedure.

5.7. NGP 20 (GRO J1744–28 or #5436)

GRO J1744–28 was discovered in 1996 as a transient source by the Burst and Transient Source Experiment on board the *Compton Gamma-Ray Observatory* (Kouveliotou et al. 1996). It is an LMXB with multiple Type II X-ray bursts and named as the Bursting Pulsar since it exhibits both bursts and pulsations (2.14 Hz with the orbital period of 11.8 days). Younes et al. (2015) present the analysis results of a simultaneous *Chandra* and *NuSTAR* observation during an outburst on 2014 March 3, which was the 3rd occurrence since its discovery. They detected the X-ray emission up to 60 keV at the Eddington flux level or higher, and the spectrum is well described by a blackbody plus a power-law model with an exponential cut-off.

In our survey the source was observed in 2013 August and July and again in 2014 August when it was relatively quiescent with no significant X-ray emission above 10 keV. The 3–10 keV X-ray luminosity at 8 kpc was about 2×10^{33} erg s^{-1}. According to quantile analysis the spectrum was consistent with $\Gamma = 3.1 \pm 0.5$ for an absorbed power-law model, making it the softest source among the *NuSTAR* detections in the GC region. This result is consistent with the earlier *Chandra* (Wijnands & Wang 2002) and *XMM-Newton* (Daigne et al. 2002) observations of the source in quiescent states, where they found the 0.5–10 keV X-ray luminosity of $\sim 3 \times 10^{33}$ erg s^{-1} and the photon index of $\Gamma_S = 2$–5.

5.8. NGP 34 (CXOUGC J174534.5–290201 or #1568)

NGP 34 is one of the two bright hard X-ray sources (the other is NGP 31) found just on the western edge of the Sgr A diffuse complex. NGP 34 was covered by seven observations, and three observations collected more than 100 net counts for the source. A main challenge for NGP 34 is in handling the diffuse background where the selection of the background aperture becomes critical (the bottom panel in Figure 7). For stacking the individual spectra of the multiple observations, we use the same aperture regions used for aperture photometry.

Figure 10(d) shows a joint model fit of non-simultaneous *NuSTAR* (black), *Chandra* (red) and *XMM-Newton* (green) spectra for an absorbed APEC model with a Gaussian line at 6.4 keV. The reduced χ^2_r is about 1.2. Including a partial covering component, which is commonly used for describing X-ray spectra from IPs (Hailey et al. 2016), improves the fit ($\chi^2_r \sim 1.1$), but the parameters for the partial covering component are not well constrained. The plasma temperature is found to be 8.6 and 12 keV with and without partial covering, respectively. The X-ray spectrum in the 6–7 keV band shows a clear sign of additional line emission besides the neutral iron line, which is also consistent with the lower plasma temperature than NGPs 3 and 4.

An absorbed power-law model fits the spectra relatively poorly even with an iron line at 6.4 keV ($\chi^2 \sim 1.5$, $\Gamma \sim 1.5$). The median energy of 11 keV (Figure 8) translates to $\Gamma = 0.7 \pm 0.2$ for an absorbed power-law model, but the high quartile ratio also implies that a thermal plasma model may be better suited for the source. Both spectral model fit and quantile analysis estimate similar 3–40 keV photon fluxes of 2.2×10^{-5} and 2.6×10^{-5} ph cm^{-2} s^{-1}, respectively. The 3–10 keV absorbed luminosity is 0.6–1.1 $\times 10^{33}$ erg s^{-1} at 8 kpc. The hard X-ray spectrum with the strong iron lines suggests that NGP 34 is likely an IP.

5.9. NGP 46 (KS 1741–293 or #5835)

KS 1741–293, discovered in 1989 by the X-ray wide field camera TTM on the Kvant module of the Mir space station (in 't Zand et al. 1991), is a transient NS LMXB, exhibiting Type I bursts. In the hard X-ray band above 20 keV, the source was detected by *INTEGRAL* for the first time (third IBIS catalog by Bird et al. 2007). Martí et al. (2007) misidentified CXOUGC J174451.0–292116 (#5824) as the *Chandra* counterpart of the source because at the time it was only the *Chandra* source consistent with the positions of the previous detections. The subsequent transient activities from KS 1741–293 (Degenaar & Wijnands 2013) indicate that the real *Chandra* counterpart is CXOUGC 174451.6–292042 (#5835), which is located about 4″ from NGP 46. Degenaar & Wijnands (2013) show the *Chandra* and *Swift* 2–10 keV flux of the source varies from 6×10^{-14} to 2×10^{-10} erg s^{-1} cm^{-2} while the photon index varies from <1 to >2. De Cesare et al. (2007) reported a 2 years monitoring of the source with *INTEGRAL* from 2003 February to 2005 May, where they observed that the hard X-ray emission above 20 keV from the source also varied by more than a factor of 10 and reached as high as 20 mCrab ($\gtrsim 10^{36}$ erg s^{-1} at 8 kpc) in the 15–30 keV band. The 5–100 keV broadband JEM-X and IBIS/ISGRI spectra were well fitted by a disk blackbody plus a cut-off power-law or a Comptonized model. In our survey, the source was covered by a single 50 ks observation in 2013 September. Unfortunately the source fell between two GR streaks of the bright neighbor 1A 1742–294. Thus its soft X-ray emission below 10 keV is somewhat uncertain, but its quiescent hard X-ray emission above 10 keV was well detected with $L_X \sim 8.9 \times 10^{33}$ erg s^{-1} at 8 kpc.

6. DISCUSSION

We have discovered 77 hard X-ray sources from the first *NuSTAR* survey of the GC region. For source detection, we introduced trial maps—new detection significance maps based on Poisson statistics-driven random chance probabilities. In Section 6.1 we explore unusually hard X-ray sources found in the trial maps of the GC region. In Section 6.2 we estimate the overall survey sensitivity. In Section 6.3 we study the significance in the lack of foreground sources in our survey. In Section 6.4 we calculate the log$N$–log$S$ distributions of the *NuSTAR* sources and illustrate how these *NuSTAR* results break some of the spectral degeneracy seen in the *Chandra* observations. In Sections 6.5 and 6.6, we explore the nature of the hard X-ray sources in the GC region with

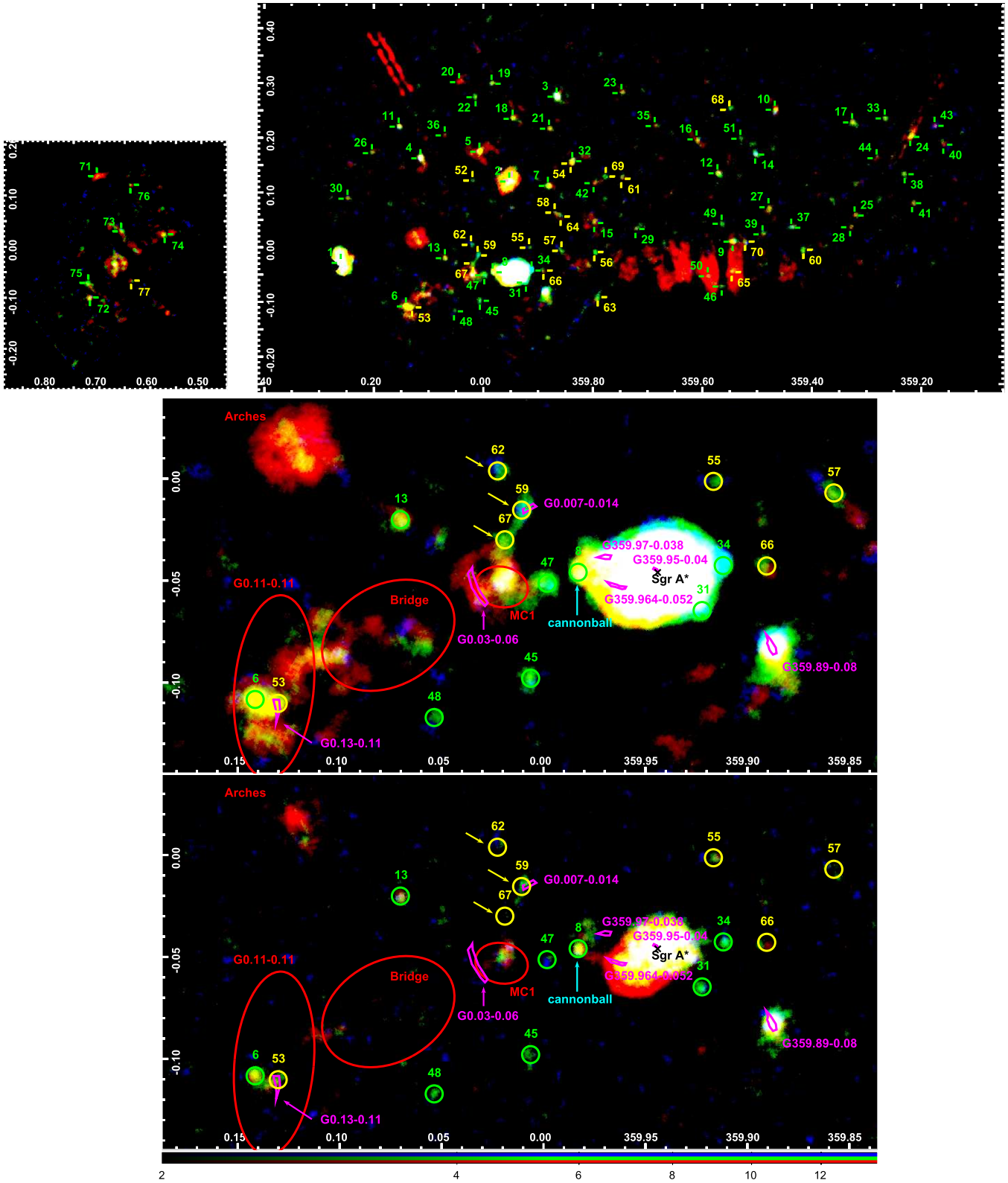

Figure 11. Three-color trial maps of the GC region using 30% PSF enclosures (top), the region around Sgr A* using 30% (middle) and 15% (bottom) enclosures. The color setting: red = 3–10 keV, green = 10–20 keV and blue = 20–40 keV. The group-1 and 2 sources are marked in green and yellow, respectively and they are labeled with the *NuSTAR* source IDs. Some of the molecular clouds and the X-ray filaments are marked with red ellipses and magenta polygons, respectively (see Ponti et al. 2015a). The yellow arrows point the three hard X-ray sources without clear soft X-ray counterparts (Section 6.1).

two possible source types—MCVs and rotationally powered pulsars.

6.1. Unusually Hard X-Ray Sources in the GC region

Figure 11 shows three-color trial maps (red: 3–10 keV, green: 10–20 keV, blue: 20–40 keV) of the GC region and a close-up region around Sgr A*. The bright X-ray emission from many diffuse and point sources near Sgr A* saturates the image in its immediate neighborhood. The trial map around Sgr A* revealed a cluster of hard X-ray sources (NGPs 59, 62 and 67; the yellow arrows in the bottom two panels of Figure 11) in the north of a Sgr A molecular cloud, MC1. These hard X-ray sources do not have obvious soft X-ray counterparts, and thus the nearby brightest and closest *Chandra* sources (CXOUGC J174542.3–285606, J174539.5–285453 and J174546.9–285608) are assigned to be potential counterparts. According to the quantile diagram in Figure 8, these sources are unusually hard with $\Gamma < 1$ for a power-law model or $kT >$ 50 keV for a single temperature thermal plasma model.

In particular, NGP 59 is located at the southern end of the small ($11'' \times 6\farcs5$) X-ray filament, G0.007–0.014 (Johnson et al. 2009; Ponti et al. 2015b). According to Johnson et al. (2009), the soft (<10 keV) X-ray spectrum of the filament has a photon index of $\Gamma_S \sim 1$ for a power-law model (albeit with a large uncertainty) and the 2–10 keV luminosity is $\sim 2 \times 10^{32}$ erg s^{-1}. This is consistent with our aperture photometry results of the *NuSTAR* source (i.e., no detection below 10 keV). Therefore, we cannot rule out the X-ray filament as the origin of the observed hard X-ray emission. The broadband (3–40 keV) spectrum of NGP 59 shows $\Gamma = 0.0 \pm 0.2$ for an absorbed power-law model. For comparison, G359.97–0.038 and Sgr A–E, two prominent non-thermal filaments in the region, show $\Gamma = 1.3$ and 2.3, respectively (Zhang et al. 2014; Nynka et al. 2015). If the *NuSTAR* detection is indeed from the X-ray filament, this is the first detection of its kind with such dominant hard (>10 keV) X-ray emission.

Besides these three sources, about a dozen *NuSTAR* sources exhibit extremely hard X-ray spectra (i.e., median energies $\gtrsim$9 keV or $\Gamma < 1$ in Figure 8, or blue sources in Figure 11). Some of these are suspected to be IPs with relatively high plasma temperatures (e.g., NGP 3, see Sections 5.3 and 6.4; see also Perez et al. 2015; Hailey et al. 2016). Of the 77 *NuSTAR* sources, 66 sources show significant X-ray emission in hard (>10 keV) X-ray bands (column 8 in Table 2).

In the hard X-ray band above 40 keV, only two significant objects, both near Sgr A*, are observed. Mori et al. (2015) explored these in the 40–79 keV trial maps generated from three observations of the Sgr A* field. One of the objects coincides with the head of G359.95–0.04, a PWN, and the other, detected at $\sim 4\sigma$ and a bit elongated in shape, does not seem to have a clear counterpart in the *Chandra* and *XMM-Newton* images. The trial maps of the full survey data show a similar result, but the morphology of the 2nd source appears less elongated.

6.2. Survey Sensitivity

We follow the recipe by Georgakakis et al. (2008) to estimate the sensitivity limit and the sky coverage of the survey. They calculated Poisson statistics-based cumulative detection probabilities expressed in an incomplete Gamma function, which is basically the same formula as Equation (1).

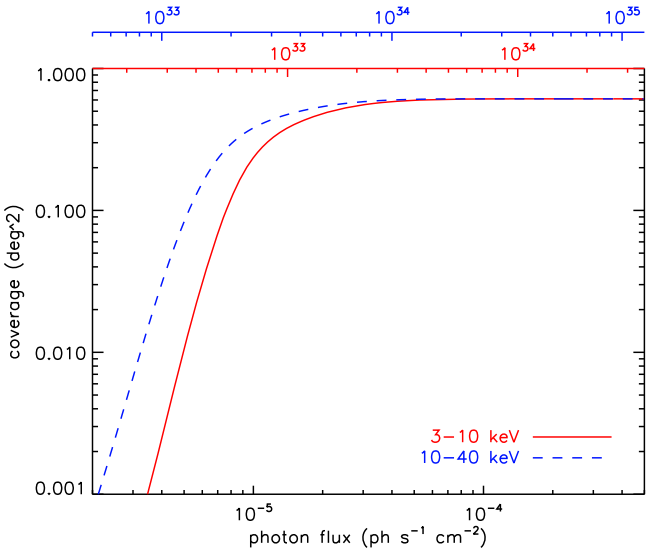

Figure 12. Sky coverage of the main GC region in the 3–10 and 10–40 keV bands as a function of absorbed photon flux. The top *x*-axis shows the corresponding X-ray luminosities at 8 kpc for each band, based on the source-averaged conversion factor (Section 6.4).

Thus, their approach is appropriate for our source search method.

For a given detection threshold (P_T), we first find the matching threshold for the total counts (N_T), then we can calculate the detection probability that a source with a given flux (f) generates the counts more than both N_T and the observed counts (N^*).

$$P(N > N_T|\lambda_S = 0,\ \lambda_B) = P_T, \tag{2}$$

$$P(N > N_0|\lambda_{S_f},\ \lambda_B) = \frac{1}{\Gamma(N_0+1)} \int_0^{\lambda_B+\lambda_{S_f}} e^{-t} t^{N_0} dt \tag{3}$$

where N_0 is $\max(N_T, N^*)$ and λ_{S_f} is the mean counts expected from a source with flux f. For a given flux f, we calculate the probability $P(N > N_0|\lambda_{S_f}, \lambda_B)$ for every pixel, and the sky coverage is given by the probability sum over all the pixels.[36] We repeat the calculation as a function of photon flux.

The observed (or absorbed) photon flux (f) is calculated as as $f = \lambda_{S_f}/(TA)$ where T is the exposure time and A the effective area. The exposure time of each sky pixel is given in the vignetting-free exposure mosaic. For the effective area, we generate an exposure map vignetted for each energy in 1 keV steps. Then for each pixel, we sum up the effective area of each energy over a given energy band, weighted by the stacked energy histogram of all the sources. In this way, for every pixel in a given energy band, we can calculate the source-spectrum averaged conversion factor from photon counts to flux.

Since we use three detection cell sizes, we use the largest detection probabilities of the three cases to get a collective sky coverage in each band. Figure 12 shows the resulting sky coverages as a function of photon flux in the 3–10 and 10–40 keV bands. The top *x*-axis shows the matching X-ray luminosities at 8 kpc using the source-averaged flux to

[36] A small difference in the normalization [$\Gamma(N+1)$ versus $\Gamma(N)$] between the above formula and Georgakakis et al. (2008) is from the fact that we use $P(N > N^*)$ for both source detection and sensitivity calculation whereas Georgakakis et al. (2008) use $P(N \geqslant N^*)$. As long as a consistent normalization is used for both source detection and sensitivity calculation, either normalization is valid.

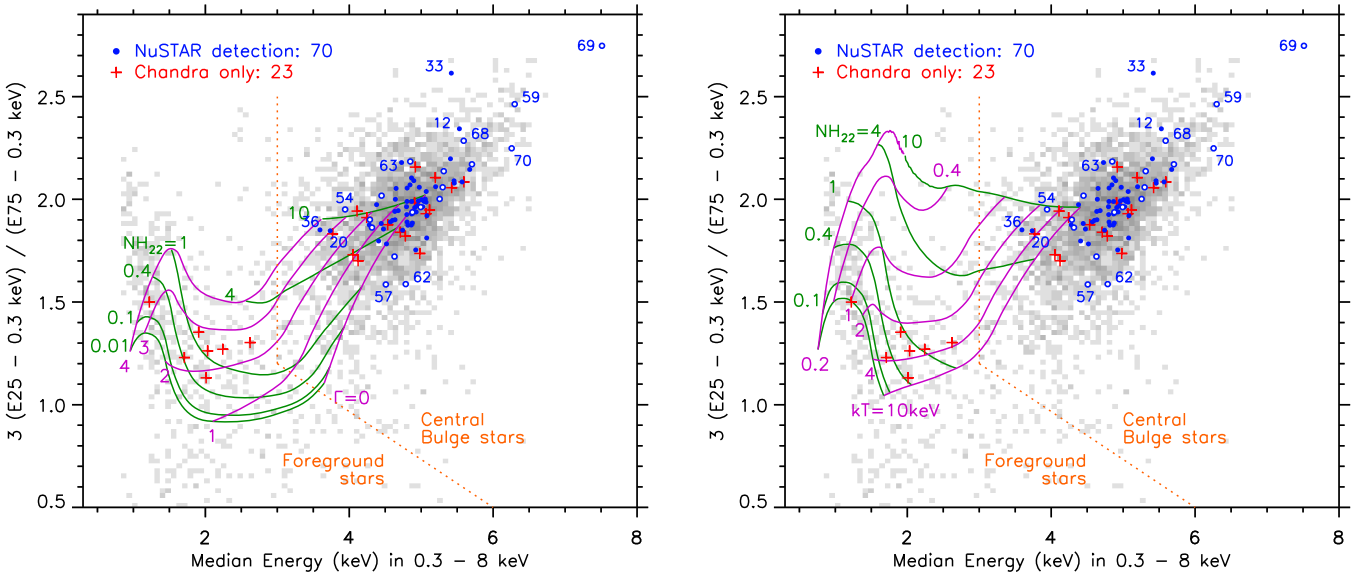

Figure 13. *Chandra* 0.3–8 keV quantile diagrams of the *Chandra* sources in the *NuSTAR* survey region. The gray density map shows the relative *Chandra* source distribution. The *NuSTAR* detections are marked with the (blue) closed circles for group 1 and the (blue) open circles for group 2. The (red) crosses show the *Chandra* sources with no *NuSTAR* detections but they are in relatively uncrowded regions and their *Chandra* 2–8 keV fluxes are high enough for *NuSTAR* detections. The grids are for power-law models with photon index $\Gamma_S = 0$, 1, 2, 3, and 4 (left) and for thermal bremsstrahlung models with $kT = 0.2$, 0.4, 1, 2, 4, and 10 keV (right). The grids also cover $N_H = 0.01$, 0.1, 0.4, 1, 4, and 10×10^{22} cm^{-2}. The (orange) dotted lines roughly separate the foreground sources from the central bulge and background AGN sources.

luminosity conversion factor (Section 6.4). The survey covers about 0.01 deg^2 at ~3–4 $\times$ 10^{32} erg s^{-1} and 0.6 deg^2 above ~2 $\times$ 10^{33} erg s^{-1} in the 3–10 keV band. In 10–40 keV, it covers about 0.01 deg^2 at ~8–9 $\times$ 10^{32} erg s^{-1} and 0.6 deg^2 above ~5 $\times$ 10^{33} erg s^{-1}.

6.3. Missing Foreground Sources?

Figure 13 shows the *Chandra* quantile diagrams in 0.3–8 keV with power-law (left) and thermal bremsstrahlung (right) model grids. The (gray) density map indicates the general distribution of *Chandra* sources with $\gtrsim$50 net counts in the *NuSTAR* survey region. A large cluster of the sources around a median energy of 5 keV and a quartile ratio of 2, where $N_H \gtrsim 4 \times 10^{22}$ cm^{-2}, are either in the central Galactic Bulge or background AGN. The (blue) circles show the *Chandra* counterparts of the *NuSTAR* detections: the closed and open circles are for the group-1 and 2 sources, respectively. The (red) crosses indicate about two dozen *Chandra* sources without *NuSTAR* detections, but their *Chandra* 2–8 keV flux should have been high enough for the *NuSTAR* detections, and they are located in relatively confusion-free sections of the survey region. Missing these relatively bright sources in the *NuSTAR* survey is not particularly surprising given the X-ray flux variability of the *Chandra* sources, but the relative ratio between the foreground and the central bulge sources is intriguing.

The diagram indicates that all the *NuSTAR* detections are either in the central bulge near the GC or background AGN. This appears true even for the group-2 sources whose *Chandra* counterparts are a bit tentative. It implies that many of them are indeed true counterparts. The lack of the foreground sources in the *NuSTAR* detections contrasts with the fact that 30% of all the *Chandra* sources in the region (the gray density map) or 30% of 22 relatively bright *Chandra* sources without *NuSTAR* detections (red crosses) are foreground sources. It shows that the *NuSTAR* selected X-ray sources in the GC region have an intrinsically harder spectral distribution than the foreground X-ray source population detected by *Chandra* in the region.

The *NuSTAR* sources provide a unique, unobscured view of the Galactic X-ray source population from the local solar neighborhood to the central bulge since the interstellar absorption to the GC (10^{22}–10^{23} cm^{-2}) has little effect in the *NuSTAR* bands. One can test if the *NuSTAR* selected X-ray sources follow the stellar population by calculating how many foreground sources we should have detected for a given detection of a central bulge source. We consider sources within 4 kpc of the Sun (i.e., $N_H \lesssim 3 \times 10^{22}$ cm^{-2}) as foreground stars and sources at distances of 6–10 kpc as bulge stars since the interstellar absorption peaks at around 4–5 kpc toward the GC (Drimmel et al. 2003). Then the relative ratio of the stellar volume density between the foreground and central bulge sources within the survey FOV is about 0.034% according to the stellar distribution model used in Muno et al. (2006) and Hong et al. (2009). Assuming that the foreground sources are closer than the central bulge sources by a factor of four on average, if the cumulative X-ray luminosity distribution follows a slope of 1.3–1.5 (M09), one can detect about ~37–64 times more foreground sources than the central bulge sources with the same flux limit. Combining these two factors, we should detect 0.013–0.022 foreground sources for every central bulge source. If we assume that about 10% of the *NuSTAR* sources are AGN (see Section 6.4), 63 out of the 70 *NuSTAR* sources found in the main GC region are near the GC. Then we expect to detect about 0.8–1.6 foreground sources among the *NuSTAR* detections. This is statistically consistent with no *NuSTAR* detection of foreground stars in the survey. Therefore, it is premature to conclude whether there is a population difference of the *NuSTAR* selected X-ray sources between the GC and other Galactic plane fields or alternatively whether there is a spectral transition in between 10^{33} erg s^{-1} at 8 kpc and 10^{32} erg s^{-1} at $\lesssim$2 kpc in the X-ray population.

On the other hand, M09, Hong et al. (2009) and Heard & Warwick (2013) suggest a possible enhancement in the soft (<10 keV) X-ray source population relative to the stellar distribution near the GC.[37] In addition, they also show a possible spectral difference between the central X-ray source population and the local field population, i.e., the average photon index (Γ_S) of the bulge sources is closer to ~1, which appears harder than accreting foreground sources. The *Chandra* results, however, are not conclusive due to the degeneracy between the high absorption and the intrinsic hardness of the X-ray spectrum in the *Chandra* energy band (see Section 6.4 and Hailey et al. 2016). The broadband coverage by *NuSTAR* can break this degeneracy and address this issue somewhat conclusively, but it requires a large increase in the survey depth or area. A. Fornasini et al. (2016, in preparation) have identified three foreground *NuSTAR* sources in the Norma region, which is still statistically consistent with our results due to low statistics. The survey area can be effectively extended by collecting serendipitous[38] foreground *NuSTAR* detections or measuring the lack thereof from other *NuSTAR* observations of Galactic plane fields in the future.

6.4. LogN–LogS Distributions

Figure 14 shows the log$N$–log$S$ distributions of the *NuSTAR* sources in the 3–10 (top) and 10–40 keV (middle and bottom) bands. The lower x-axis is the observed photon flux (F_X) and the upper axis the observed X-ray luminosity (L_X) in the same band at 8 kpc. The conversion factor between the two x-axes is an average value of the conversion factors for all the sources. Specifically, $F_X \sim 10^{-5}$ ph cm^{-2} s^{-1} corresponds to $L_X \sim 7.1 \times 10^{32}$ erg s^{-1} in the 3–10 keV band and $L_X \sim 2.5 \times 10^{33}$ erg s^{-1} in 10–40 keV. The top panel also shows the AGN distribution using a photon index of 1.7 with $N_H = 1.2 \times 10^{23}$ cm^{-2} based on the extragalactic survey results by Kim et al. (2007). We expect about 10% of the *NuSTAR* detections to be AGN.

In order to estimate the systematic errors, we compare the distributions prepared in three different methods: case (A) uses both group-1 and 2 sources with the photon fluxes based on the the first aperture sets, case (B) is the same but with the second aperture sets, and case (C) is for only the group-1 sources with the first aperture sets. The largest difference among the three cases in each flux bin is considered to be the systematic errors of the log$N$–log$S$ distributions. The statistical errors for case (C) are shown in the gray shade in Figure 14. A logarithmic linear fit to case (C) is shown by the yellow solid line, which follows a relation of $N(>S) = N_0(S/S_0)^{-\alpha}$. For comparison, we also overplot the the *Chandra* 0.5–8 keV log$N$–log$S$ distribution (M09) scaled to the *NuSTAR* bands for six different spectral models: $\Gamma = 0.5$, 1 and 2 for absorbed power-law models and $kT = 10$, 20 and 50 keV for single temperature APEC models. Note that M09 assumed $\Gamma = 0.5$. We assume $N_H = 6 \times 10^{22}$ cm^{-2} for all the models above. Since all of the *NuSTAR* detections have *Chandra* counterparts or at least candidates, both *Chandra* and *NuSTAR* distributions should be consistent with each other.

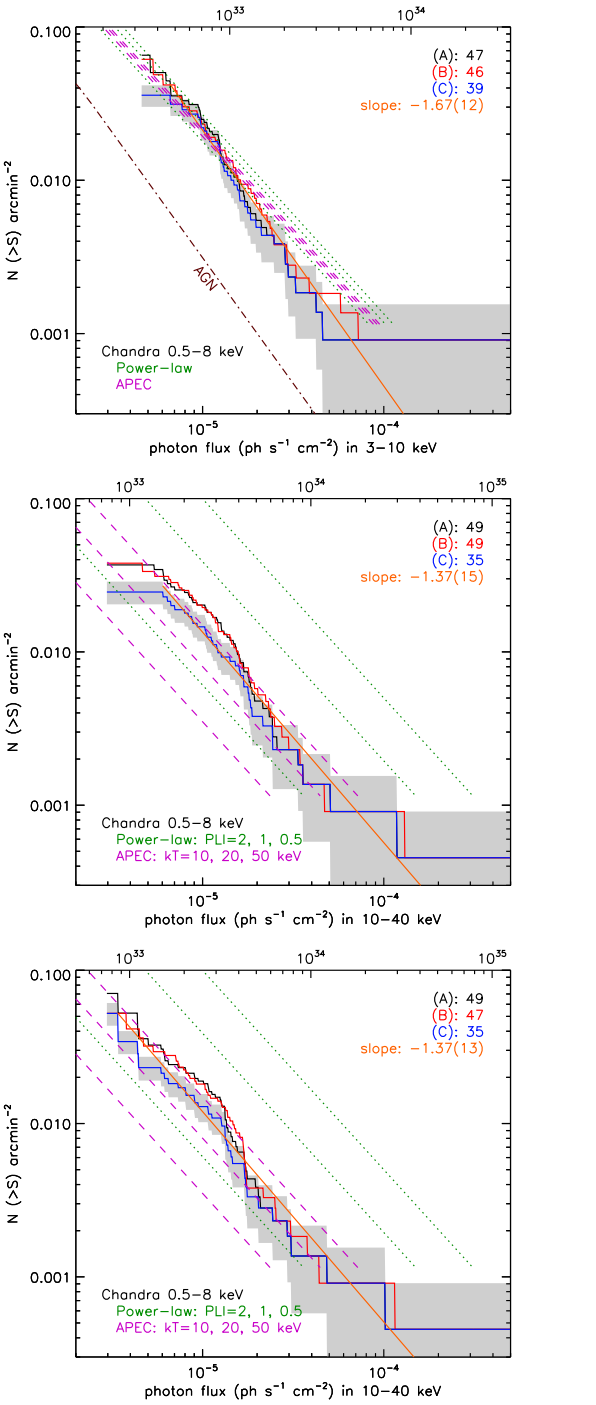

Figure 14. Comparison of the *NuSTAR* 3–10 keV (top) and 10–40 keV log$N$–log$S$ distributions (middle and bottom) with the *Chandra* 0.5–8 keV log$N$–log$S$ distribution. The top two panels use the model-based flux estimation, and the bottom panel use the non-parametric flux estimation (Sections 4.4 and 6.4). (A-black) The group-1 and 2 sources with the first aperture sets (see Section 4.1), (B-red) with the second aperture sets and (C-blue) the group-1 sources with the first aperture sets. The gray region shows the statistical errors for (C) and the (yellow) solid line is the best fit for (C). The (green) dotted and (magenta) dashed lines show the *Chandra* 0.5–8 keV log$N$–log$S$ distribution from M09: green dotted lines are for power-law models with $\Gamma = 2$, 1 and 0.5 (from bottom to top) and magenta dashed lines are for APEC with $kT = 10$, 20 and 50 keV (from bottom to top). The brown dashed-dot line in the top panel is AGN (Kim et al. 2007).

[37] In the case of Heard & Warwick (2013), the claim was made for a lower luminosity limit (~10^{31} erg s^{-1}) than this survey or the other two studies (~10^{32} erg s^{-1}).

[38] For a fair comparison, the target of each observation should not be counted unless the observation is a part of a blind survey.

The *NuSTAR* 3–10 keV log*N*–log*S* distribution has a slope of $\alpha \sim 1.7 \pm 0.1$. It shows some deficit relative to the *Chandra* distribution since the *NuSTAR* detections did miss some bright *Chandra* sources likely due to on-going variability but they match within 1.5σ of the statistical uncertainties. It is clear that the soft energy band below 10 keV is insensitive to the assumed spectral models in converting the *Chandra* distribution, in part due to the similarity between the two bands in comparison given the absorption toward the GC (i.e., the fluxes below 2 keV do not contribute much).

In the 10–40 keV band, the luminosity distribution of the *NuSTAR* sources shows a slope of 1.4 ± 0.1. Unlike the 3–10 keV band, in 10–40 keV, the assumption of the average spectral shape in translating the 0.5–8 keV *Chandra* distribution makes a significant difference. For an absorbed power-law model, the average photon index Γ should be somewhere in between 1.5 and 2 or for an absorbed single-temperature APEC model, the average temperature kT should be somewhere in between 20 and 50 keV in order for the two distributions to match. This result is also consistent with the photon index distribution in Figure 9.

Since the flux of each source in the log*N*–log*S* distribution (the middle panel in Figure 14) is calculated for a power-law model with the median energy-based photon index used in Figure 9, one can argue that the consistency in the overall photon index distribution between the two figures may not be the result of two entirely independent analyses. For a sanity check, we re-derive the log*N*–log*S* distribution using the flux values that are calculated non-parametrically and model-independently (Section 4.4), as shown in the bottom panel in Figure 14. The non-parametric flux estimation results in a bit lower flux values for the faint sources. This is in part because dividing a relatively small number of X-ray counts from faint sources into each small energy bin of 1 keV step can lead to some signal loss in the non-parametric calculation. On the other hand, the model-based calculation tends to overestimate the flux of the faint sources depending on how accurately the assumed model represents the true X-ray spectrum of each source. Regardless of some differences near the faint end, the *NuSTAR* 10–40 keV log*N*–log*S* distributions of both model-based and model-independent fluxes require the similar average spectral types for X-ray emission of the *NuSTAR* sources in order to be consistent with the *Chandra* distribution.

With the *Chandra* energy band alone, it is hard to constrain the X-ray spectra of the GC X-ray sources, but the *NuSTAR* observations put a tighter constraint on the plasma temperature for a thermal model or photon index.[39]

6.5. Are MCVs Dominant in NuSTAR X-Ray Sources?

Of nine relatively bright *NuSTAR* sources in Section 5, four are NS XB systems, one is a run-away pulsar, another is suspected to a BH or NS XB and the other three are suspected to be MCVs. Of 15 *NuSTAR* sources with their *Chandra* spectra model-fitted to search for the iron lines (Section 4.5), 11 sources show a sign of the iron lines, seven of which have the broadband photon index $\Gamma < 1.5$, whereas two in the other four sources without the iron lines have $\Gamma < 1.5$. Among the combined 24 sources, about 70% of the relatively hard sources with $\Gamma < 1.5$ show the iron lines, whereas only about 40% of the relatively soft sources with $\Gamma > 1.5$ show the iron lines. The iron lines, combined with a hard continuum ($\Gamma \lesssim 1.5$ or $\Gamma_S \lesssim 1$ for an absorbed power-law model), is a good indicator of a MCV rather than a NS or BH XB. The relatively high percentage of the iron lines[40] among the sources with the hard continuum ($\Gamma \lesssim 1.5$) indicates that the *NuSTAR* source population contain a large fraction of MCVs, at least 40% of the above 24 sources. Or if we consider all the sources with the iron lines as MCVs, the fraction increases to ~60%. Then roughly the other 40% can be BH or NS XBs.

On the other hand, (Degenaar & Wijnands 2010; Degenaar et al. 2012) detected 17 transients within the central 1.2 deg^2 of the GC based on long term monitoring programs of the GC region using *Chandra* and *Swift*. These programs cover more or less the complete sample of the BH or NS XBs with recurring bursts on a timescale of less than a decade. Among 14 in our survey field, four were detected by *NuSTAR* (Table 4), seven were unresolved in the Sgr A diffuse complex, and the other three were undetected. The relatively small number of transients observed in the GC region indiciate that the fraction of BH or NS XBs is likely much smaller than 40%.

As seen in Figure 9, the 3–40 keV luminosities at 8 kpc of the *NuSTAR* sources are mostly in a range of 10^{33-34} erg s^{-1}, where both quiescent NS or BH XBs and bright MCVs can be found. The broadband spectral properties of the *NuSTAR* sources show that both of these types can contribute significantly to the *NuSTAR* source population. We expect that the relative fraction of MCVs in the remaining fainter *NuSTAR* sources can be much higher as their luminosity range falls into a more typical luminosity range of IPs. Therefore, the overall fraction of MCVs in the *NuSTAR* sources is expected be greater than ~60%.

A key result of our survey is that the hard X-ray spectra of the *NuSTAR* sources in the GC region are consistent with the apparent diffuse, central hard X-ray emission (CHXE) found by Perez et al. (2015). A leading scenarios is that the diffuse hard X-ray emission is from 1000–10,000 unresolved IPs with high mass WDs, which can produce high temperature plasma above 30 keV. For a single temperature model, such a high temperature translates to WD masses of $\gtrsim 0.8 M_\odot$, which is much higher than the average WD mass of $\sim 0.6\ M_\odot$ in MCVs that are suspected to be responsible for the Galactic Ridge X-ray emission (GRXE). For instance, a broadband (2–50 keV) analysis of the GRXE from the *Suzaku* observations of the Galactic Bulge within 1°–3° of the GC also shows a lower plasma temperature (12–15 keV) for the overall combined X-ray spectra (Yuasa et al. 2012). Bright MCVs found in the Norma region by A. Fornasini et al. (2016, in preparation) also exhibit a noticeably lower plasma temperature for a single temperature model (<20 keV in the Norma region versus >20 keV in the GC region). Note hard X-ray CVs selected by *INTEGRAL*/IBIS in the field do show an average temperature of $kT \sim 22$ keV (Landi et al. 2009), but given the limited band

[39] By "photon indices," we mean an equivalent photon index for a simple power-law model. As seen with the cut-off power-law model (the right panel of Figure 8), the photon indices can be easily skewed with additional parameters when a more complex model is employed. The soft band (<10 keV) photon index (Γ_s) of ~0.5 observed by *Chandra* can be consistent with the broadband Γ of 1.5 observed by *NuSTAR* if there is a high energy cut-off at around 10 keV in the power-law spectrum.

[40] A typical EW of the iron lines from MCVs ranges from ~150 to 300 eV (Ezuka & Ishida 1999). On the other hands, quiescent XBs ($\lesssim 10^{33}$ erg s^{-1}) do not appear to exhibit detectable Fe line emission ($\lesssim$50–120 eV) although their sample size is small (e.g., Bradley et al. 2007; Chakrabarty et al. 2014; Rana et al. 2016).

width on the soft X-ray side ($\gtrsim$15 keV), CVs detected by *INTEGRAL*/IBIS or *Swift*/BAT likely have a selection bias toward high plasma temperature, wheres the boardband coverage by *NuSTAR* is relatively free of such a bias.

A possible scenario resulting in high mass (>0.8 $M_{\odot}$) WDs in the CVs near the GC is that the GC region harbors a large number of >4 $M_{\odot}$ B-stars, compared to the field, given the WD initial–final mass relation according to Andrews et al. (2015). Hailey et al. (2016) argue that the excess B-star population needed to explain high WD masses is within the large uncertainty of the expected population in the GC region. On the other hand, the average mass of the WD in the non-magnetic CVs or isolated magnetic WDs are about $0.8M_{\odot}$ (Ferrario et al. 2015; Wijnen et al. 2015). In addition, there is no clear evidence for high mass progenitors for the WDs in CVs (Zorotovic et al. 2011). Since the highly magnetized, isolated WDs are considered to be products of binary evolution, perhaps the binary evolution may be responsible for high mass WDs in the CVs. Then the relatively low WD mass from the X-ray observations of the field is more unusual than the projected high mass of the WD based on the X-ray spectral analysis of the sources in the GC region.

The similarity in the broadband X-ray spectra of the CHXE and the *NuSTAR* sources in this survey reinforces the scenario that (1) the X-ray population in the GC region is predominantly MCVs but also with a significant fraction of NS and BH XBs, and (2) the GC region also harbors an increasingly higher fraction of MCVs with high WD masses that produce harder X-rays than those in other regions in the plane.

6.6. MSPs or Young Pulsars in NuSTAR X-Ray Sources?

Another interesting proposal for the CHXE by Perez et al. (2015) is that it can be the result of the unresolved non-thermal emission from a large population of millisecond pulsars (MSPs). To explain the total observed luminosity of 2×10^{34} erg s^{-1} with rotationally powered systems, about 4000 MSPs would be needed with an average non-thermal X-ray ($L_{n,X}$) luminosity of 5×10^{30} erg s^{-1} under the assumption of $L_{n,X} \sim 10^{-4}\ \dot{E}$ according to Takata et al. (2012), where $\dot{E}$ is the spin-down power.

The recent *Fermi* observations of excess gamma-ray emission in the inner galaxy (Goodenough & Hooper 2009; Hooper & Goodenough 2011) triggered a series of debates regarding its origin: e.g., dark matter annihilation (e.g., Hooper & Linden 2011) or a collection of unresolved MSPs (e.g., Abazajian & Kaplinghat 2012) or young pulsars (O'Leary et al. 2015). Lee et al. (2015) presented evidence of unresolved gamma-ray point sources in the *Fermi* observations of the inner galaxy by demonstrating that a simple pure Poisson distribution is inadequate to explain the observed distribution of the excess gamma-ray photons within the central few degrees. If gamma-ray point sources are required to explain the excess, MSPs and young pulsars become the leading candidates given their dominance in the Galactic *Fermi* source population.

According to Hooper et al. (2013), the number of the MSPs required to explain the gamma-ray excess exceed by a factor of 10 what is projected from the observed field population. Cholis et al. (2014) also argue against MSPs as the source of the gamma-ray excess, based on the paucity of the resolved sources within the central 10° of the GC. Contrarily Brandt & Kocsis (2015) proposed the Galactic Bulge as a giant collection of disrupted globular clusters, which can naturally lead to an enhancement of MSPs and subsequently explain the excess gamma-ray emission. In fact, Hooper et al. (2013) pointed out that the inner tens of parsecs from the GC could have high MSP population as massive globular clusters, and thus the model by Brandt & Kocsis (2015) effectively extends the region with a high population of MSPs to a few kpc scale (~10°). On the other hand, O'Leary et al. (2015) argue that the excess gamma-ray emission can be explained with a reasonable number of young pulsars, given their relatively bright gamma-ray emission (Abdo et al. 2013). However, it appears difficult to explain the drastic difference in scale and morphology between the CHXE (asymmetric, parsec scale) and the excess gamma-ray emission (symmetric, kpc scale) with a single type of the source population, either MSPs or young pulsars.

In the case of the *NuSTAR* X-ray sources in our survey, the 10–40 keV X-ray luminosities for the majority are $\sim 10^{33-34}$ erg s^{-1}. It is not straightforward to estimate the gamma-ray luminosity (L_{γ}) of rotationally powered pulsars from its X-ray luminosity (L_X), but if we assume that the hard X-ray emission from the *NuSTAR* X-ray sources is a non-thermal component of rotationally powered pulsars, we can roughly estimate L_{γ} through the spin-down power (Marelli et al. 2011), with the relation $L_{n,X} \sim 10^{-4}\ \dot{E}$. Then, the expected L_{γ} for many of the *NuSTAR* sources exceeds 10^{35-37} erg s^{-1}, which corresponds to 10^{-11}–10^{-9} erg s^{-1} cm^{-2} at 8 kpc.

According to the *Fermi* pulsar catalog (Abdo et al. 2013), the brightest MSPs have $L_{\gamma} \sim 10^{34}$ erg s^{-1}, and the *NuSTAR* sources are much too bright to be the typical MSPs found by *Fermi*. Young pulsars are brighter than MSPs, but the expected L_{γ} of the *NuSTAR* sources are still near or above the brightest young pulsars observed by *Fermi*. Since the 50% completeness limit of individual source detection at the GC is about 4×10^{-11} erg s^{-1} cm^{-2} according to O'Leary et al. (2015). the expected L_{γ} of the brightest *NuSTAR* sources is large enough for *Fermi* to resolve individually. Although the *NuSTAR* sources in this survey would be likely spatially confused for *Fermi*, similar hard X-ray sources in the vicinity of the region, if they are rotationally powered pulsars, could have been resolved by *Fermi* as suggested in Cholis et al. (2014). In addition, at least some young pulsars are expected to be associated with PWNe with observable soft (<10 keV) X-ray filaments, depending on their ages (e.g., Muno et al. 2008, suggested young pulsars created in the last 300 kyr based on 34 X-ray filaments), but the majority of the *NuSTAR* sources do not show any association with the soft (<10 keV) X-ray filaments. Therefore, at least the bright *NuSTAR* X-ray sources in our catalog are believed not to be typical rotationally powered pulsars unless the *NuSTAR* X-ray sources are unusual pulsars with much higher-than-usual X-ray luminosities for the given spin-down power.

7. SUMMARY AND FUTURE WORK

1. We have discovered 70 hard X-ray sources in the 0.6 deg^2 region around the GC and 7 in the Sgr B2 cloud field. Of the 77 sources, 66 sources show significant X-ray emission in hard (>10 keV) X-ray bands.
2. The broadband (3–40 keV) energy quantiles of the *NuSTAR* sources show that for a power-law model the majority of the sources have photon indices of $\Gamma = 1$–2 and about 20% with $\Gamma < 1$.

3. The 3–10 keV log$N$–log$S$ distribution of the *NuSTAR* sources is in a good agreement with the 0.5–8 keV *Chandra* distribution of the GC region.
4. The *NuSTAR* 10–40 keV and *Chandra* 0.5–8 keV log$N$–log$S$ distributions match if the average photon index (Γ) of the *NuSTAR* sources is in between 1.5 and 2 for a power-law model or the plasma temperature lies between 20 and 50 keV for a single temperature APEC model.
5. For an absorbed power-law model, the average soft (<10 keV) band photon index (Γ_S) of the *Chandra* sources in the GC region was estimated to be 0.5–1 (M09; Hong et al. 2009), which is smaller than the broadband (3–40 keV) photon index (Γ) measured here for the *NuSTAR* sources. The limited *Chandra* energy band is responsible for the discrepancy, but if the X-ray spectra of the GC region X-ray sources have an exponential cut-off at ~10 keV, the apparent photon indices of the *Chandra* and *NuSTAR* spectra match.
6. The spectral analysis of the relatively bright 24 sources suggests that MCVs comprise >40%–60% of the total, and NS or BH XBs can make up the rest. The fraction of MCVs among the fainter sources is likely higher (>60%).
7. The *NuSTAR* sources in the GC region exhibit higher plasma temperatures than the hard X-ray sources in the field including the Norma region by A. Fornasini et al. (2016, in preparation). If MCVs comprise a large majority of the *NuSTAR* sources in the GC region, the observed plasma temperature range translates to a WD mass of $\gtrsim$0.8 $M_\odot$, which is higher than the field average of ~0.5 $M_\odot$ (Hailey et al. 2016).
8. A large population of IPs with higher mass WDs can explain the average X-ray spectrum of the *NuSTAR* sources in this survey as well as the CHXE discovered by Perez et al. (2015).
9. If the *NuSTAR* X-ray sources in the GC region are rotationally powered pulsars, their expected L_γ exceeds typical values of both MSPs and young pulsars observed by *Fermi*. Therefore, the *NuSTAR* X-ray sources in this survey do not likely contain many rotationally powered pulsars.
10. The *NuSTAR* detections lack foreground sources, which is significantly different from the *Chandra* source population but it is still consistent with the stellar population, given the sensitivity and coverage limitations of the present survey.

It is essential to continue monitoring of the GC region for understanding the nature of the hard X-ray sources and the GC region as a whole. To acquire broadband X-ray spectra of several *NuSTAR* sources with high photon statistics, deep exposures of selected regions in block A is planned under the *NuSTAR* legacy program.

This work was supported under NASA Contract No. NNG08FD60C, and made use of data from the *NuSTAR* mission, a project led by the California Institute of Technology, managed by the Jet Propulsion Laboratory, and funded by the National Aeronautics and Space Administration. We thank the *NuSTAR* Operations, Software and Calibration teams for support with the execution and analysis of these observations. We thank G. Ponti for careful reading and suggestions of the manuscript. This research has made use of the *NuSTAR* Data Analysis Software (NuSTARDAS) jointly developed by the ASI Science Data Center (ASDC, Italy) and the California Institute of Technology (USA). J. Hong acknowledges support from NASA/APRA grant NNX14AD59G. R. Krivonos acknowledges support from Russian Science Foundation through grant 14-22-00271. F.E. Bauer acknowledges support from CONICYT-Chile (Basal-CATA PFB-06/2007, FONDECYT 1141218, "EMBIGGEN" Anillo ACT1101), and the Ministry of Economy, Development, and Tourism's Millennium Science Initiative through grant IC120009, awarded to The Millennium Institute of Astrophysics, MAS. S. Zhang is supported by NASA Headquarters under the NASA Earth and Space Science Fellowship Program—Grant NNX13AM31. D. Barret acknowledges support from the French Space Agency (CNES).

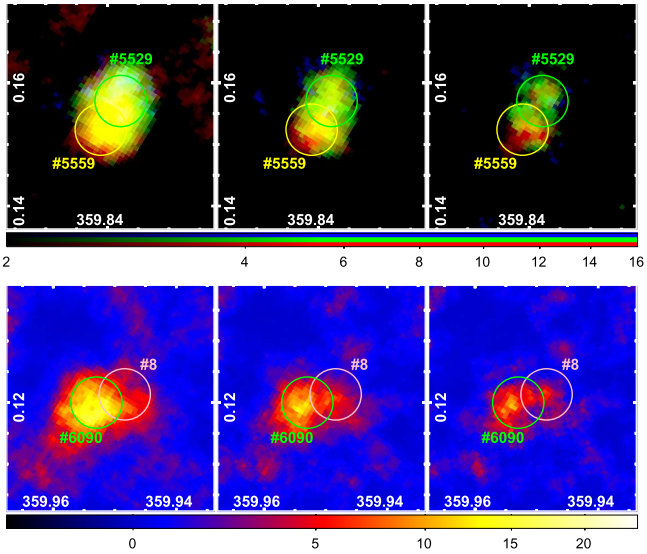

Figure 15. Resolving CXOUGC J174437.1–285934 (*Chandra* ID #5529 or NGP 32) and CXOUGC J174438.7–285933 (#5559 or NGP 54) (top) and GRS 1741.9–2853 (#6090 or NGP 2) vs. CXOUGC J174501.3–285501 (#8) (bottom). The images are the trial maps of 30%, 20% and 15% PSF enclosures from left to right. The top panels are the three color trial maps (red: 3–10 keV, green: 10–20 keV, blue: 20–40 keV) and the bottom panels are in 20–40 keV. The circles show 15″ radii around the *Chandra* source positions.

APPENDIX

A.1. Resolving Power of the NuSTAR Optics

Two *Chandra* sources, CXOUGC J174437.1–285934 and CXOUGC J174438.7–285933, are located about 20″ apart from each other and show similar photon fluxes in the 2–8 keV band (M09). In *NuSTAR*, the three-color trial maps in the same region show two bright spots (NGPs 32 and 54) with distinct X-ray colors, which are also separated by about 20″ (top panel in Figure 15). The separations between these two *NuSTAR* spots and the *Chandra* sources are about 5″–6″. Based on the relative proximity to the *Chandra* sources, we associate NGP 32 to CXOUGC J174437.1–285934 and NGP 54 to CXOUGC J 174438.7–285933.

Five observations covered the region: two observations do not have bright sources to define a clear astrometric correction, and the other three require <5″ boresight shifts. Since the boresight shifts are mostly less than 10″ (Figure 1), we believe that the 20″ separation between the two spots in the trial map is too large for an astrometric error. In addition, trial maps made

of the three observations with astrometric corrections show similar results (not shown). On the other hand, the largest offset between the *NuSTAR* and *Chandra* sources in Table 2 is about 13.″5, and thus it is very unlikely but possible that the combination of a large astrometric error and a large statistics-driven positional uncertainty may produce an artificial 20″ separation. If so, then the source must have been experiencing a remarkable spectral variation (see below). Considering these factors, we assign the brighter of the two in group 1 and the other in group 2.

The *NuSTAR* quantile diagram shows that the X-ray spectrum of NGP 32 is harder and more consistent with a power-law model while NGP 54 is softer and more consistent with a thermal model (Figure 8). The *Chandra* quantile diagram (Figure 13 in Section 6.3) also shows that CXOUGC J174437.1–285934 has a harder X-ray spectrum ($\Gamma_S \sim 1$) than CXOUGC J174438.7–285933 ($\Gamma_S \sim 3$).

The 20–40 keV trial map shows another similar case of two nearby sources (GRS 1741.9–2853 versus CXOUGC J174501.3–285501, 17″ apart). Since GRS 1741.9–2853 is predominantly brighter at low energies below 20 keV, an additional peak is only resolved in the 20–40 keV trial map (the bottom panel in Figure 15, too faint above 40 keV). The significance of the new spot in the trial map appears to be roughly consistent with the 2–10 keV flux differences between the two *Chandra* sources (a factor of ∼20 according to M09). The burst-only data of GRS 1741.9–2853 do not show any peak with a similar significance near CXOUGC J174501.3–285501, implying that the peak in the survey trial maps is not likely an artifact of the large PSF wings of GRS 1741.9–2853. On the other hand, there is no clear sign of CXOUGC J174501.3–285501 in the *NuSTAR* data during the quiescent period of GRS 1741.9–2853. Our re-analysis of the *Chandra* archival data does not show any significant sign of X-ray signals at the location of CXOUGC J174501.3–285501, which questions the validity of the *Chandra* detection. Without the *Chandra* counterpart, a marginal detection near the threshold in one energy band technically does not meet our source selection criteria. Therefore, we excluded CXOUGC J174501.3–285501 as part of the *NuSTAR* detections. Confirmation of CXOUGC J174501.3–285501 as a real detection will require additional *Chandra* observations with GRS 1741.9–2853 near the aimpoint when GRS 1741.9–2853 is relatively faint.

A.2. Diffuse Emission

The trial maps generated with fixed-size detection cells retain diffuse emission structures in convolution with the PSF at the scales of the cell sizes. The prominent diffuse structures seen in the trial maps include the Sgr A complex, a few molecular clouds (Mori et al. 2015) and X-ray filaments including G359.89–0.08 (Sgr A–E; Zhang et al. 2014), the Arches Cluster (Krivonos et al. 2014), G359.97–0.038 (Nynka et al. 2015), and the Sgr B2 cloud (Zhang et al. 2015). These regions are excluded in our point source analysis. Since the trial maps show the emission significance in general, it would require iterative forward modeling with a proper emission morphology to extract the flux or intensity of the emission structure from a trial map, which is beyond the scope of this paper. On the other hand, the trial maps reveal a general trend of emission morphology more clearly than raw images.

The three color trial map of the Arches cluster (the middle panel in Figure 11) shows an elongated bright hard X-ray streak embedded in a soft circular diffuse structure (see a wavelet analysis in Krivonos et al. 2014). In the MC1 region, the trial map (the bottom panel in Figure 11) shows a possible spatial separation between the soft and hard X-ray emission. The soft X-ray emission is more extended along Galactic latitude and closer to Sgr A*, whereas the hard X-ray emission is more central with respect to the Galactic plane and further away from Sgr A*. The separation is too small (about 7″) to rule out systematic artifacts, but it does support the idea of a morphological spectral variation in the region. For instance, Clavel et al. (2013) claimed a detection of spatial variation in the evolution of the Fe K_α line and argued for an X-ray reflection nebula model (see also Ponti et al. 2013, p. 331) where the X-ray emission from the cloud was triggered by bright flares of Sgr A* in the past. See Mori et al. (2015) for an in-depth analysis of the *NuSTAR* observations of MC1.

REFERENCES

Abazajian, K. N., & Kaplinghat, M. 2012, PhRvD, 86, 083511
Abdo, A. A., Ajello, M., Allafort, A., et al. 2013, ApJS, 208, 17
Anders, E., & Grevesse, N. 1989, GeCoA, 53, 197
Andrews, J. J., Agüeros, M. A., Gianninas, A., et al. 2015, ApJ, 815, 63
Barrière, N. M., Krivonos, R., Tomsick, J. A., et al. 2015, ApJ, 799, 123
Barrière, N. M., Tomsick, J. A., Baganoff, F. K., et al. 2014, ApJ, 786, 46
Bélanger, G., Goldwurm, A., Renaud, M., et al. 2006, ApJ, 636, 275
Bird, A. J., Malizia, A., Bazzano, A., et al. 2007, ApJS, 170, 175
Bodaghee, A., Tomsick, J. A., Krivonos, R., et al. 2014, ApJ, 791, 68
Bradley, C. K., Hynes, R. I., Kong, A. K. H., et al. 2007, ApJ, 667, 427
Brandt, T. D., & Kocsis, B. 2015, ApJ, 812, 15
Broos, P. S., Townsley, L. K., Feigelson, E. D., et al. 2010, ApJ, 714, 1582
Buccheri, R., Bennett, K., Bignami, G. F., et al. 1983, A&A, 128, 245
Chakrabarty, D., Tomsick, J. A., Grefenstette, B. W., et al. 2014, ApJ, 797, 92
Cholis, I., Hooper, D., & Linden, T. 2014, arXiv:1407.5583
Clavel, M., Terrier, R., Goldwurm, A., et al. 2013, A&A, 558, A32
Cocchi, M., Bazzano, A., Natalucci, L., et al. 1999, A&A, 346, L45
Daigne, F., Goldoni, P., Ferrando, P., et al. 2002, A&A, 386, 531
De Cesare, G., Bazzano, A., Martínez Núñez, S., et al. 2007, MNRAS, 380, 615
Degenaar, N., & Wijnands, R. 2010, A&A, 524, A69
Degenaar, N., & Wijnands, R. 2013, in IAU Symp., Feeding Compact Objects: Accretion on All Scales, 290, 113
Degenaar, N., Wijnands, R., Cackett, E. M., et al. 2012, A&A, 545, A49
Degenaar, N., Wijnands, R., Reynolds, M. T., et al. 2014, in IAU Symp., The Galactic Center: Feeding and Feedback in a Normal Galactic Nucleus, 303, 315
Drimmel, R., Cabrera-Lavers, A., & López-Corredoira, M. 2003, A&A, 409, 205
Ezuka, H., & Ishida, M. 1999, ApJS, 120, 277
Ferrario, L., de Martino, D., & Gänsicke, B. T. 2015, SSRv, 191, 111
Freeman, P. E., Kashyap, V., Rosner, R., & Lamb, D. Q. 2002, ApJS, 138, 185
Georgakakis, A., Nandra, K., Laird, E. S., Aird, J., & Trichas, M. 2008, MNRAS, 388, 1205
Goodenough, L., & Hooper, D. 2009, arXiv:0910.2998
Hailey, C., Mori, K., Perez, K., et al. 2016, arXiv:1605.06066
Harp, D. I., Liebe, C. C., Craig, W., et al. 2010, Proc. SPIE, 7738, 77380Z
Harrison, F. A., Craig, W. W., Christensen, F. E., et al. 2013, ApJ, 770, 103
Heard, V., & Warwick, R. S. 2013, MNRAS, 428, 3462
Hong, J. 2012, MNRAS, 427, 1633
Hong, J., Schlegel, E. M., & Grindlay, J. E. 2004, ApJ, 614, 508
Hong, J. S., van den Berg, M., Grindlay, J. E., & Laycock, S. 2009, ApJ, 706, 223
Hooper, D., Cholis, I., Linden, T., Siegal-Gaskins, J. M., & Slatyer, T. R. 2013, PhRvD, 88, 083009
Hooper, D., & Goodenough, L. 2011, PhLB, 697, 412
Hooper, D., & Linden, T. 2011, PhRvD, 84, 123005
in 't Zand, J. J. M., Heise, J., Brinkman, A. C., et al. 1991, AdSpR, 11, 187
Johnson, S. P., Dong, H., & Wang, Q. D. 2009, MNRAS, 399, 1429
Kashyap, V. L., van Dyk, D. A., Connors, A., et al. 2010, ApJ, 719, 900
Kaspi, V. M., Archibald, R. F., Bhalerao, V., et al. 2014, ApJ, 786, 84

Kim, M., Wilkes, B. J., Kim, D.-W., et al. 2007, ApJ, 659, 29
Kouveliotou, C., van Paradijs, J., Fishman, G. J., et al. 1996, Natur, 379, 799
Krivonos, R. A., Tomsick, J. A., Bauer, F. E., et al. 2014, ApJ, 781, 107
Landi, R., Bassani, L., Dean, A. J., et al. 2009, MNRAS, 392, 630
Laycock, S., Grindlay, J., van den Berg, M., et al. 2005, ApJL, 634, L53
Lee, S. K., Lisanti, M., Safdi, B. R., Slatyer, T. R., & Xue, W. 2015, arXiv:1506.05124
Lotti, S., Natalucci, L., Mori, K., et al. 2016, ApJ, 822, 57
Madsen, K. K., Harrison, F. A., Markwardt, C. B., et al. 2015, ApJS, 220, 8
Marelli, M., De Luca, A., & Caraveo, P. A. 2011, ApJ, 733, 82
Martí, J., Combi, J. A., Pérez-Ramírez, D., et al. 2007, A&A, 462, 1065
Mauerhan, J. C., Cotera, A., Dong, H., et al. 2010, ApJ, 725, 188
Mori, K., Gotthelf, E. V., Dufour, F., et al. 2014, ApJ, 793, 88
Mori, K., Gotthelf, E. V., Zhang, S., et al. 2013, ApJL, 770, L23
Mori, K., Hailey, C. J., Krivonos, R., et al. 2015, ApJ, 814, 94
Muno, M. P., Baganoff, F. K., Bautz, M. W., et al. 2003, ApJ, 589, 225
Muno, M. P., Baganoff, F. K., Brandt, W. N., Morris, M. R., & Starck, J.-L. 2008, ApJ, 673, 251
Muno, M. P., Bauer, F. E., Baganoff, F. K., et al. 2009, ApJS, 181, 110 (M09)
Muno, M. P., Bauer, F. E., Bandyopadhyay, R. M., & Wang, Q. D. 2006, ApJS, 165, 173
Nishiyama, S., Nagata, T., Tamura, M., et al. 2008, ApJ, 680, 1174
Nynka, M., Hailey, C. J., Mori, K., et al. 2013, ApJL, 778, L31
Nynka, M., Hailey, C. J., Zhang, S., et al. 2015, ApJ, 800, 119
O'Leary, R. M., Kistler, M. D., Kerr, M., & Dexter, J. 2015, arXiv:1504.02477
Park, S., Muno, M. P., Baganoff, F. K., et al. 2005, ApJ, 631, 964
Park, T., Kashyap, V. L., Siemiginowska, A., et al. 2006, ApJ, 652, 610
Perez, K., Hailey, C. J., Bauer, F. E., et al. 2015, Natur, 520, 646
Ponti, G., Morris, M. R., Terrier, R., et al. 2015a, MNRAS, 453, 172
Ponti, G., Morris, M. R., Terrier, R., & Goldwurm, A. 2013, in Astrophysics and Space Science Proc., Cosmic Rays in Star-Forming Environments, ed. D. F. Torres & O. Reimer (Berlin: Springer), 34
Ponti, G., Morris, M. R., Terrier, R., et al. 2015b, MNRAS, 453, 172
Rana, V., Loh, A., Corbel, S., et al. 2016, ApJ, 821, 103
Revnivtsev, M., Sazonov, S., Churazov, E., et al. 2009, Natur, 458, 1142
Revnivtsev, M., Sazonov, S., Forman, W., Churazov, E., & Sunyaev, R. 2011, MNRAS, 414, 495
Sunyaev, R. 1990, IAUC, 5104, 1
Takata, J., Cheng, K. S., & Taam, R. E. 2012, ApJ, 745, 100
Townsley, L. K., Broos, P. S., Corcoran, M. F., et al. 2011, ApJS, 194, 1
van den Berg, M., Hong, J. S., & Grindlay, J. E. 2009, ApJ, 700, 1702
Wang, Q. D., Gotthelf, E. V., & Lang, C. C. 2002, Natur, 415, 148
Watson, M. G., Willingale, R., Hertz, P., & Grindlay, J. E. 1981, ApJ, 250, 142
Weisskopf, M. C., Wu, K., Trimble, V., et al. 2007, ApJ, 657, 1026
Wijnands, R., & Wang, Q. D. 2002, ApJL, 568, L93
Wijnen, T. P. G., Zorotovic, M., & Schreiber, M. R. 2015, A&A, 577, A143
Wik, D. R., Hornstrup, A., Molendi, S., et al. 2014, ApJ, 792, 48
Younes, G., Kouveliotou, C., Grefenstette, B. W., et al. 2015, ApJ, 804, 43
Yuasa, T., Makishima, K., & Nakazawa, K. 2012, ApJ, 753, 129
Zhang, S., Hailey, C. J., Baganoff, F. K., et al. 2014, ApJ, 784, 6
Zhang, S., Hailey, C. J., Mori, K., et al. 2015, arXiv:1507.08740
Zhao, J.-H., Morris, M. R., & Goss, W. M. 2013, ApJ, 777, 146
Zorotovic, M., Schreiber, M. R., Gänsicke, B. T., et al. 2011, A&A, 536, L3